

# **Title: The human digital twin brain in the resting state and in action**

**Authors:** Wenlian Lu <sup>1,†</sup>, Qibao Zheng <sup>1,†</sup>, Ningsheng Xu <sup>1</sup>, Jianfeng Feng <sup>1,2,3,4,5,\*</sup> and DTB Consortium

## **Affiliations:**

<sup>1</sup> Institute of Science and Technology for Brain-Inspired Intelligence, Fudan University, Shanghai, China

<sup>2</sup> Key Laboratory of Computational Neuroscience and Brain-Inspired Intelligence (Fudan University), Ministry of Education, China

<sup>3</sup> Shanghai Center for Mathematical Sciences, Fudan University, Shanghai, China

<sup>4</sup> Department of Computer Science, University of Warwick, Coventry, United Kingdom

<sup>5</sup> Zhangjiang Fudan International Innovation Center, Shanghai, China

† These authors contributed equally to this work.

\*Corresponding author. Email: [jianfeng64@gmail.com](mailto:jianfeng64@gmail.com)

**Abstract:** We simulate the human brain at the scale of up to 86 billion neurons, i.e., digital twin brain (DTB), which mimics certain aspects of its biological counterpart both in the resting state and in action. A novel routing communication layout between 10,000 GPUs to implement simulations and a hierarchical mesoscale data assimilation method to be capable to achieve more than trillions of parameters from the estimated hyperparameters are developed. The constructed DTB is able to track the its resting-state biological counterpart with a very high correlation (0.9). The DTB provides a testbed for various ‘dry’ experiments in neuroscience and medicine, and illustrated in two examples: exploring the information flow in our brain, and testing deep brain stimulation mechanisms. Finally, we enable the DTB to interact with environments by demonstrating some possible applications in vision and auditory tasks, and validate the power of DTB with achieving significant correlation with the experimental counterparts.

**One-Sentence Summary:** We develop a human digital twin brain with novel routing communication and hierarchical mesoscale data assimilation methods.

## Main Text:

Despite progress in brain science, computer science and mathematics, it has been a great challenge to simulate a spiking neuronal network of human brain scale, up to of 86B neurons (1), in an intensively biological-based interconnected structure by a currently available high-performance computer with reasonable performance, which is resource demanding and for which a simple brute-force approach is doomed to fail (2-6). However, in neuroscience, we cannot directly measure the activity of billions of neurons in a healthy human brain. Therefore, even if we had the data of each neuron's activity available and the resource to simulate such a model of human-brain scale, we are still lack of a mathematical tool to reverse engineer the complex neuronal networks, which basically requires fitting at least trillions of parameters (7). This is essentially important to deploy the model for brain and intelligence study.

More related to this work, the European Human Brain Project (HBP), at its beginning, aimed to simulate a biological brain: a mouse or a rat brain, and in the end, produced two types of digital brains. The SpiNNaker (8), the ARM-based simulation engine, as well as the others such as NEST (9), can perform simulations at cellular level of brains (10). It has been remarkably used in performing some simulations, in particular, networks of local circuits such as the striatum circuit (11). The TVB, on the other hand, uses the mean field approach and aims to simulate the brain with its local field potentials for each brain region and is currently undergoing a large clinical trial on brain diseases such as epilepsy (12-14).

Currently the data which we can directly measure for a whole human brain is the blood-oxygen-level-dependent (BOLD) signal for each voxel (a human brain typically has around 100,000 voxels), the fibre connections between each measured voxel and the structural data which essentially is the neuronal density (i.e., the number of neurons) for each voxel (Fig 1A, left panel). With these available data, we intend to construct a digital twin brain (DTB) as similar as possible to its biological counterpart. In this study, the DTB is a spiking neural network model composed of up to 86 billion interacting neurons and 10 trillion synapses for spike communications (i.e., the number of total neurons in a human brain). Computationally, DTB is available at three resolution scales, from low to high resolution, the brain region level, the voxel level, and the micro-column level (Fig. 1A, middle panel). 10,000 graphical processing units (GPU) cards (AMD, 16 GB Memory) are required to simulate the DTB with 86 billion neurons. By proposing optimization algorithms for data processing and spike communications (9), we have achieved a time-to-solution of 60 with average firing rate 17.5 HZ for diverse trials, i.e., 60 secs are required for DTB to complete 1 sec biological computation in human brain (See the Supplemental Report). Mathematically, combined with hierarchal mesoscale data assimilation algorithm, DTB is fitted to the human brain in the resting state and in action. With our DTB platform, two experiments are conducted, a "dry" experiment to explore the information flow related to cognitive neuroscience, and a virtual deep brain stimulation (DBS) in medicine (Fig. 1A, right panel). Two tasks, for visual and auditory processing, are performed with the DTB (Fig. 1A right top panel).

## Results

### *DTB at a glance*

The DTB gives methods and platform of neuromorphic computing and statistic inference and comprises of two components. One is to construct and simulate neuronal network of human-brain scale and intensively biological data driven structure on general GPU-based HPC with appreciable performance. The other is to fit the brain resting-state experiment data and mimic

real-world functional experiment tasks by a proposed hierarchical mesoscale data assimilation method.

The network structure in DTB is constructed in accordance with the connectivity characteristics of a human brain (Fig. 1B). Firstly, the simulated number of neurons in a neuronal population (region or voxel or micro-column) is proportional to the grey matter volume obtained from the T1-weighted MRI image (Fig. 1B, top row) and the l. Two types of neurons (excitatory neurons and inhibitory neurons) are included here and the ratio of the number of excitatory neurons to that of inhibitory neurons in each neuronal population is set as 4:1 (with necessary variation in the micro-column model). Each neuron is described by the Leaky integrate and fire (LIF) model with four synaptic currents (AMAP, NMDA, GABA<sub>A</sub>, GABA<sub>B</sub>). Second, the structural connection probability between a pair of neuronal populations is estimated by the row-normalized fibre counts obtained from the Diffusion Tensor Image (DTI) (Fig. 1B, middle left row). It is assumed that the long-range connections between neuronal populations are only excitatory since the inhibitory connections tend to be local. Thirdly, the connection within each neuronal population inside a micro-column is based on neuroanatomy data (15) (Fig 1B, bottom row). Based on these data and knowledge (16,17), we can derive a weighted directed graph of neuronal populations (Fig. 1B, right column). Finally, with the predefined network size (86B) and in-degree scale (100), the large-scale interconnected neuronal network as DTB can be constructed. The supplemental materials provide details.

Due to the thousands of memory accesses, spike package communications and update calculations per neuron in a millisecond, the simulation cost of DTB is very expensive. In addition, the inhomogeneous distribution of the numbers of neurons and synapses achieved from the biological structure data (T1 and DTI) causes extreme imbalance of data loading and communication. To meet the requirement of low-latency communication between GPUs for the DTB simulation, we first propose a partitioning algorithm and a two-level routing (Fig 1C) method to balance the data traffic and reduce the degree of GPU connections (Fig. 1C). More specifically, instead of assigning neurons to multiple GPUs according to their biological layout, we apply the partitioning algorithm to assign a set of neurons that have strong communication between each other to the same GPU to take advantage of the faster communication speed within a GPU, which reduces the data traffic between GPUs (Fig. 1C, left column). However, the inter-GPU communications are imbalanced, which may lead to network congestion. For example, due to GPUs No. 1 to No. 8 simultaneously communicating with GPU No.12, the total traffic amount exceeds its maximum capacity, introducing extra latency due to waiting for communication. To address this question, we further proposed a control scheme with a two-level routing structure (Fig. 1C, right column). We split multiple GPUs into different groups. Then for each node (node  $k$ ), either as a source or a destination, to communicate with GPUs from a different group, it has to send one copy of duplicate spikes to routing GPU (1, ...,  $r_k$ ), which serves as a transfer station to multicast the spike copies to the corresponding destination GPUs. An iterative greedy algorithm is employed to assign GPUs to different groups to ensure high cohesion for traffic within a group and low coupling for traffic in different groups. Compared to the original one-level routing communication (shown in light red/blue colour) in Fig. 1C, our new two-level routing method (shown in dark red/blue colour) reduces the number of the total source (destination) connections down to a magnitude order of its square root (18).

From the simulation of DTB, we can collect the neural activities (i.e., spike raster) and the corresponding firing rates (Fig. 1D, left column). The time series of the BOLD signal from

each ROI/voxel are formulated by the Balloon-Windkessel model (19), and generate the simulated BOLD signals (Fig. 1D, bottom row). To fit the experimental BOLD signal (Fig. 1D, top row) with the simulated BOLD signal (Fig. 1D, bottom row), we proposed a framework of hierarchal mesoscale data assimilation (HMDA) to estimate the model parameters, more specifically, the synaptic conductance of each neuron. However, due to the huge amount of parameters (more than 10 trillion parameters for 86B neurons in total), we take each region of interest (ROI), for instance, the brain region, voxel or each layer of the micro column structure according to the resolution of the network model, and assume that the conductance parameters of the same type of the neurons in the same ROI follow the same distribution, or, equivalently, share the same hyper-parameters. The aim of the data assimilation is to statistically infer the brain-scale neuronal network by tracking the BOLD signals. The hyper-parameters are estimated and each conductance value is sampled according to the distribution with the hyper-parameters.

By this way, we show that the highly steadily similar BOLD signals are achieved by simulating a neuronal network of an arbitrarily larger scale than the assimilated model, for instance, the human-brain scale model of 86B neurons, with the network structure sampled from the same network model as the assimilated model and conduct values sampled from the distribution of the estimated hyperparameters. Therefore, the DTB, equipped with the hierarchal mesoscale data assimilation, can be used to conduct digital experiments to explore the phenomena at neuronal and synaptic level (dry experiment). Particular, the assimilated model can be validated by mimicing the cognitive action task by simulating the brain by the assimilated model, compared with the results of the real-world experiments (in-action experiment). See Supplementary Materials for all details.

### ***DTB in the resting state***

As an illustrative example of DTB (the micro-column version), the cortex voxel is composed of six layers: L1, L2/3, L4, L5 and L6, equipped with excitatory and inhibitory neurons. Inside each voxel, the excitatory neurons and inhibitory neurons are balanced for excitatory post-synaptic potentials (AMPA and NMDA) and inhibitory post-synaptic potentials (GABA<sub>A</sub> and GABA<sub>B</sub>). The cortico-cortical connections from each voxel are excitatory connections via the L5 only (Fig. 2A). The training phase is rapid, with a small transition period of around 10 seconds (demonstrated for the BOLD signal from one of the voxels in V1 in Fig. 2B). It is shown that the data assimilation can perfectly track the BOLD signals and there is a high similarity between the biological brain and the assimilated DTB, with the averaged correlation coefficients of the time course of all voxels between the simulation of DTB after data assimilation and the experimental counterpart achieving 0.90 (Fig. 2D). For each brain region in the AAL template (20), the averaged correlation coefficients of the voxels in all brain regions are over 0.8 (Fig. 2C). The brain regions with the lowest correlation coefficients lie in the subcortex, for instance, the hippocampus and amygdala (AMYG) with a value around 0.8 (Fig. 2C), possibly due to that the lower DTI quality in the subcortex than in the cortex. It is also shown that as the number of neurons in the DTB increases, the correlation coefficients improve steadily, in that the variance of the correlation coefficients (over 100 repeated simulations of the DTB) significantly decreases with respect to the scale of the DTB (Fig. 2G). We highlighted that the voxel-wise estimated hyperparameters can be used to achieve an assimilated model of 86 billion neurons by sampling the dynamic conductance parameters from these estimated hyperparameters and the simulated resting-state BOLD signals of

assimilated model of 86 billion neurons also achieved a very high coherence with the experimental BOLD signals of the Pearson correlation over 0.9 (See the Supplementary Report).

Second, with the DTB the averaged firing rate of all neurons in each brain region can be assessed, where the primary visual cortical area V1 has the highest firing rate (Fig. 2E), as reported in PET data (21). On the other hand, the posterior cingulate gyrus (PCG) has the lowest firing rate, which is again confirmed in recent data (22). The detailed spikes and firing rate for inhibitory and excitatory neurons in each voxel even in the micro-column layer are assessable with DTB (Fig. 2F). In the best-fitted resting state DTB, one can see that the firing rate of the inhibitory neuronal population is generally higher than that of the excitatory population and the inhibitory population of the L2/3 is highest within the micro-column (19.4 spikes/s).

Finally, to understand the dynamics of the DTB in the resting state, the spectrogram of all brain regions of the simulated local field potentials for 2 seconds is calculated (Fig. 2H). It is shown that the Amygdala has the highest gamma power in the resting state (Fig. 2H, as indicated in red). On the other hand, the region with the lowest gamma power is the superior temporal pole (TPOsup, as indicated in blue), which is consistent with resting-state fMRI results showing that the magnitude of the high frequency band of the BOLD signal is lower in frontal, parietal, and occipital cortices compared to subcortical areas (23).

### ***Experiments with DTB***

It is well known that it is impossible to directly measure information processing at the neuronal level of resolution for the whole human brain. With the DTB, however, we can now uncover the information processing by carrying out ‘dry’ experiments. The first example is to explore the information processing in the whole human brain with a visual or an auditory stimulus (see Supplementary Materials). In the second example, we demonstrate how to utilize DTB to explore the underlying mechanisms and test the deep brain stimulation setup for an individual brain. In contrast with the information flow studied for the human brain with low temporal-spatial resolution (for instance MRI, MEG/EEG (24)), the DTB broadens the view of complete brain pathway and real-time evolution in a higher resolution.

We inject a pulsed current to excitatory cells in the calcarine (CAL, primary visual cortex) with a 50 ms duration to mimic the visual input in our daily perceptual information (Fig. 3A). From the ‘BOLD’ signal of period 800 ms acquired from the simulations, it can be seen that almost no significant change happens in the brain except the input region (CAL) being activated (red box) (Fig. 3B). In comparison, if look at the higher resolution such as neuronal firing rates (Fig. 3C) and local field potential (LFP) (Fig. 3D) in DTB, the activities change significantly with respect to stimuli as shown by three different methods that we employ to track the information flow (see Supplemental Material for details).

Firstly, from the perspective of the onset time of the local field potential (LFP), different brain regions exhibit different response: deflections are faster and stronger compared with those positions farther away from visual stimuli. The visual stimulus evoked wave calculated by ranking the spike onset in response to the stimuli travels across the brain (Fig 3.D). Secondly, to assess the duration of the response to a stimulus, we use the average activation strength (25) during a 50 ms window in the post-stimulus state compared to the pre-stimulus state for each voxel (see supplementary materials). We perform a permutation test by implementing a Wilcoxon rank Sum Test ( $p < 0.005$ ). Visual activation occurs in the primary visual cortical

areas, such as the lingual gyrus and cuneus, and then transmits to the temporal lobe and parietal lobe, corresponding to the ventral and dorsal pathways (Fig. 3E). The hippocampus which integrates the incoming information from the ventral and dorsal pathways is also activated (Fig. 3E). Some frontal areas such as OFC and Broca's area are also activated.

Finally, to analyse the spatio-temporal dynamics of the experimental data, here we adopt the optical flow estimation methods (26) with a spatial total variational penalty to construct the velocity vector field at each time step (one millisecond frame) (Fig. 3F, also see Supplementary Materials). From the map of principal component (PC1) of velocity amplitude (Fig. 3G), the highly activated regions (larger than the third quartile of PC1) are circled, which more or less coincides with the ventral pathway (27) (Fig. 3E). The values of PC1 before and after a stimulus onset indicate the sudden changes of the velocity field when the stimulus is on and off (Fig. 3G). The correlation of the information flow (stream line, Fig. 3H left panel) and the gradient directions for the resting state and DTB with stimulus show that in the resting state, the information is more biased: more information flows from top-down than bottom-up, while with the visual stimulus, the bottom-up information flow is increased while the top-down one is decreased, demonstrating the information flow from primary visual regions to higher functional regions (Fig. 3H, right panel). These phenomena correspond well to the previous research results (28).

To provide some insights into the underlying mechanism of brain-computer interface, we implement virtual deep brain stimulus (DBS) in the DTB to explore the relationship between the stimulus paradigms and cortical responses, by injecting a pulsed current at 125 Hz with 1 ms pulse width, which is gamma-distributed with parameters taking values as 5 and 6/5, to each neuron in the sub-thalamic nucleus (STN) (Fig. 4A). The activities of neurons in the left STN (i.e., the spikes and firing rate) and their corresponding LFPs show huge differences with and without these pulsed currents (Fig. 4B). The analysis of power spectral density (PSD) further suggests that the pulsed current affects the power at different frequency bands differently (Fig. 4C). It affects the low frequency bands more than the high frequency bands (Fig. 4C). There is high similarity between the percentage of DTI connections from STN to each Parkinson's disease-related brain region (29) and the differences of firing rate with and without DBS in these regions (Fig. 4D & E), reflecting the importance of DTI connections in DTB. Again, similar to STN, the pulsed current mainly affected the low frequency band (i.e., delta and theta band) activity in these regions (Fig. 4F). To assess the overall impact of DBS on the neural circuit, we apply Granger causality to our data with the package developed by our previous research (30, 31). It is clearly shown that when the pulsed current is on, the overall connection is dramatically driven by the STN (Fig. 4G). We next test the outcome of different input frequencies with different setups: one with identical pulse width and the other with the identical quantity of electricity. It can be seen that the reduced power at low frequency activity is a monotonic function of the input frequency, which might indicate the importance of the high frequency input in pulsed current (Fig. 4H). Although pulsed current, used as DBS, for the treatment of Parkinson's disease is one of the most successful stories for neuronal modulation, the exact mechanism is not known (32). Our DTB gives an unprecedented platform to address the issues which are impossible to work on using a biological brain.

### ***DTB in action***

Herein, we go a step further to show the potential of DTB for applications to validate the availability of the DTB. To achieve this, we utilize the HMDA method to assimilate the sensory input brain regions and voxels from the experimental BOLD signal obtained by functional MRI

(fMRI). Then, we use the assimilated brain regions working as the input source that are inserted to the whole brain network for specific subjects. Then, we collect the BOLD signals from the specific output brain regions (voxels) in his/her individual DTB to predict his/her task scores (Fig. 5A, also see Supplemental Materials for the details). Two tasks were implemented in our DTB: evaluation tasks for visual and auditory stimuli (Fig. 5B). Here we present the visual task and one can refer to Supplemental Materials for the auditory task (fig. S8). In the visual task, we assimilate each voxel in the calcarine cortex (CAL, 868 voxels), as well as the inferior frontal gyrus (opercular part, IFGoperc, 248 voxels) and supramarginal gyrus (SMG, 368 voxels), in the AAL template as the visual input ROIs (Fig. 5A, also see Supplemental Materials for details). It turns out the input signal that is decoded can be precise. We use the simulated BOLD signals of all voxels except the input regions, i.e. CAL, IFGoperc and SMGs to estimate the value in the visual evaluation task (Fig. 5G).

First, we assimilate the DTB of subject 1 with the experimental BOLD signals in the visual evaluation task. After obtaining the inputs for the three regions at voxel level, we then inject the inputs to a DTB in resting state by taking the averaging value of all conductance. It turns out that the DTB can reach a correlation coefficient of 0.73 for the visual task at the voxel level (Fig. 5C top panel) and 0.77 at the regional level (Fig. 5C bottom panel and Fig. 5D). Note that the subcortical regions such as the pallidum again have the lowest correlation. In general, the DTB in the visual evaluation task for subject 1 fits well with its biological counterpart. Second, we applied the inputs in the three areas obtained in subject 1 to two other subjects' DTB (Fig. 5E) and obtained their activation patterns. Fig. 5 F shows the comparison of DTB activation patterns and actual activation patterns. Although it is in general in agreement with each other, it is clearly seen that there are discrepancies. With all these activation patterns available, a simple linear regression model via LASSO is utilized to predict the visual evaluation scores by the simulated BOLD time course of the DTB. With a total number of 51 pictures for the three subjects (each subject evaluates 17 pictures), we trained the LASSO model to perform the prediction task with a z-score range from -3 to 3. Finally, the Pearson correlation coefficient of 0.58 between the predicted scores and the experimental measures was achieved by leave-one-out cross-validation (Fig. 5G).

## Discussion

The DTB presents the ability to carry out the simulation of neuronal networks of human-brain scale, for instance up to 86B neurons, and a reverse engineering approach to reconstruct spiking neuronal networks at the cellular level and using as constraints biological data including DTI, T1 and functional MRI data (33). We found that extremely large-scale neuromorphic simulation is both communication- and memory-access-intensive with highly parallel computations. Hence, we argue that the GPU-based HPC system would be better alternative than CPU-based system as used in most state-of-the-art works (4-6) when simulating neuronal networks of human-brain-scale in a general-purposed HPC. In addition, inhomogeneity of the network structure obtained from the real-world biological data causes extreme imbalance of data loading and communication, which presents the major challenge (1-3).

The hierarchal mesoscale data assimilation method can well track the BOLD signals with a correlation coefficient of 0.90 for the resting state and 0.77 for action between biological brain and DTB. Therein, the DTB is a rational platform for us to carry out 'dry' and 'in-silicon' experiments on individual brains, with potential for applications in both cognitive neuroscience and in medicine. We have demonstrated how to test the deep brain stimulation setup in our

DTB platform. Finally, the availability of the DTB validated by carrying out visual and auditory evaluation tasks with reverse engineering to decode the input signals, which again demonstrated a remarkable property of DTB.

Although the computational approach is claimed to be the third pillar of scientific methodology (34), we have not seen a successful platform for whole human brain simulation yet. The reason is clear from what we have done here: it needs both mathematical (soft) and network design (hardware) breakthroughs. By developing the hierarchical mesoscale data assimilation (HMDA) method, we have successfully estimated the 10 trillion parameters. We are not arguing that DTB developed here is the unique solution, but it is one of the solutions. The DTB platform is the first promising one which can offer a global view of how the human brain works, other than implementing models of attention, memory, emotion, decision, object recognition etc. separately (35).

The DTB also can serve as a platform for digitally trying and testing various cognitive and medical approaches. As another similar project, TVB, has shown the successful application of such models in medicine (epilepsy) (12), and the DTB can also directly be used in testing various medical setups. In our first attempt here, we have tried to assess the impact of DBS for a healthy subject. In the following study, we are working on a Parkinson's patient and will compare our simulations with medical treatments. In the dry, visual stimulus, experiment, we have applied a current to the visual area to assess the information flow in DTB at neuronal, LFP, and BOLD scale with the millisecond resolution. Certainly, we cannot access data of the whole human brain in response to stimuli at the millisecond and neuronal scale data. Hence our platform opens up, for the first time in the literature, the possibility of testing various experiments in a simulated human brain. SpiNNaker, one of the most advanced spiking neuronal networks, has successfully been used by many researchers (11). Definitely, the DTB platform should be open for scientists all over the world to perform their 'dry' experiments and test their hypotheses.

For a system such as DTB to be lasting, we have to find real applications in real life. In the action experiment, we tried one such example with the data from one subject, we can then simulate the reaction from many subjects when they face the same stimuli. This is a typical scenario of making a decision based upon a population of participants: joined-up thinking. Using the same approach, we can soon have a population of 1000 brains and then we can make a decision/evaluation based upon all of these 1000 brains.

This is the first version of DTB and it naturally raises more questions than we can answer here. First of all, we only have limited biological data which we can use as constraints. For example, DTI data is directionless and we all know that the brain network topologies are definitely directed (16). As a consequence, the information flow is less constrained than it should be. In reality, we actually have both BOLD data and simultaneously recorded MEG/EEG data, which might help us increase the reliability at a fine temporal scale. Second, the limits of the bandwidths of both communication and memory access contribute to the bottleneck of the scale of brain simulation. For example, the average synaptic degree of each neuron is set to 100, which is widely known to be as large as 1000-10000 in human brain (17).

To warrant the applicability of the DTB, at this moment, we are still working on intuitive user interfaces, guidelines and interfaces for model construction, and generally to address a range of more fundamental infrastructure aspects. For example, if we or others have developed a more realistic, biophysical-based hippocampus model, it should be easy to insert the model

into our whole DTB model to replace the LIF model based by the hippocampus model. Last but not the least, the current model needs a considerable amount of computational power to run, and a hardware implementation should be our future aims.

## References

1. S. Herculano-Houzel, The human brain in numbers: a linearly scaled-up primate brain. *Frontiers in Human Neuroscience* **3**, 1 (2009).
2. K. Amunts, T. Lippert, Brain research challenges supercomputing. *Science* **374**, 1054-1055 (2021).
3. A. Mehonic, A. J. Kenyon, Brain-inspired computing needs a master plan. *Nature* **604**, 255-260 (2022).
4. R. Ananthanarayanan, et al., The cat is out of the bag: cortical simulations with  $10^9$  neurons,  $10^{13}$  synapses, in *Proceedings of the Conference on High Performance Computing Networking, Storage and Analysis, ser. SC '09*, 63:1–63:12 (2009).
5. R. Preissl et al., Compass: A scalable simulator for an architecture for Cognitive Computing. *SC '12: Proceedings of the International Conference on High Performance Computing, Networking, Storage and Analysis IEEE*, (2013).
6. T. Yamazaki, J. Igarashi, H. Yamaura, Human-scale Brain Simulation via Supercomputer: A Case Study on the Cerebellum. *Neuroscience* **462**, 235–246 (2021).
7. K. Hao. (MIT Technology Review, accessed, 2020).
8. S. B. Furber, F. Galluppi, S. Temple, L. A. Plana, The SpiNNaker Project. *Proceedings of the IEEE* **102**, 652-665 (2014).
9. S. Spreizer et al. NEST Desktop, an Educational Application for Neuroscience. *eNeuro* **8**, eneuro.0274-21 (2021).
10. G. T. Einevoll, et al. The scientific case for brain simulations. *Neuron* **102**, 735–744 (2019).
11. B. Sen-Bhattacharya et al., Building a Spiking Neural Network Model of the Basal Ganglia on SpiNNaker. *IEEE Transactions on Cognitive and Developmental Systems* **10**, 823-836 (2018).
12. M. Schirner et al., Brain modelling as a service: the virtual brain on EBRAINS. (2021).
13. P. Sanz Leon et al., The Virtual Brain: a simulator of primate brain network dynamics. *Front Neuroinform* **7**, 10 (2013).
14. M. M. Woodman et al., Integrating neuroinformatics tools in TheVirtualBrain. *Front Neuroinform* **8**, 36 (2014).
15. T. Binzegger, R. J. Douglas, K. A. Martin, A quantitative map of the circuit of cat primary visual cortex. *J Neurosci* **24**, 8441-8453 (2004).X. Du et al., A Low-Latency Communication Design for Brain Simulations. *IEEE Network* **36**, 8-15 (2022).
16. D. S. Modha, R. Singh. Network architecture of the long-distance pathways in the macaque brain. *Proc. Natl. Acad. Sci. U.S.A.* **107(30)**, 13485-13490 (2010).
17. C. Zimmer. 100 Trillion Connections: New Efforts Probe and Map the Brain's Detailed Architecture. *Scientific American*, **304(1)**, 58-63 (2011).
18. X. Du et al., A Low-Latency Communication Design for Brain Simulations. *IEEE Network* **36**, 8-15 (2022).
19. K. J. Friston, A. Mechelli, R. Turner, C. J. Price, Nonlinear responses in fMRI: the Balloon model, Volterra kernels, and other hemodynamics. *Neuroimage* **12**, 466-477 (2000).

20. N. Tzourio-Mazoyer *et al.*, Automated anatomical labeling of activations in SPM using a macroscopic anatomical parcellation of the MNI MRI single-subject brain. *Neuroimage* **15**, 273-289 (2002).
21. F. Hyder *et al.*, Uniform distributions of glucose oxidation and oxygen extraction in gray matter of normal human brain: No evidence of regional differences of aerobic glycolysis. *J Cereb Blood Flow Metab* **36**, 903-916 (2016).
22. H. Wang *et al.*, Population-specific brain [(18)F]-FDG PET templates of Chinese subjects for statistical parametric mapping. *Sci Data* **8**, 305 (2021).
23. A. T. Baria, M. N. Baliki, T. Parrish, A. V. Apkarian, Anatomical and Functional Assemblies of Brain BOLD Oscillations. *Journal of Neuroscience* **31**, 7910-7919 (2011).
24. A. Korzeniewska, M. Manczak, M. Kaminski, K. J. Blinowska, S. Kasicki, Determination of information flow direction among brain structures by a modified directed transfer function (dDTF) method. *J Neurosci Meth* **125**, 195-207 (2003).
25. G. Deco *et al.*, Perturbation of whole-brain dynamics in silico reveals mechanistic differences between brain states. *Neuroimage* **169**, 46-56 (2018).
26. B. K. P. Horn, B. G. Schunck, Determining Optical-Flow. *Artif Intell* **17**, 185-203 (1981).
27. M. A. Goodale, A. D. Milner, Separate Visual Pathways for Perception and Action. *Trends in Neurosciences* **15**, 20-25 (1992).
28. T. J. Buschman, E. K. Miller, Top-down versus bottom-up control of attention in the prefrontal and posterior parietal cortices. *Science* **315**, 1860-1862 (2007).
29. C. H. Tai *et al.*, Electrophysiological and metabolic evidence that high-frequency stimulation of the subthalamic nucleus bridles neuronal activity in the subthalamic nucleus and the substantia nigra reticulata. *FASEB J* **17**, 1820-1830 (2003).
30. Q. Luo, T. Ge, F. Grabenhorst, J. Feng, E. T. Rolls, Attention-dependent modulation of cortical taste circuits revealed by Granger causality with signal-dependent noise. *PLoS Comput Biol* **9**, e1003265 (2013).
31. Q. Luo *et al.*, Spatio-temporal Granger causality: a new framework. *Neuroimage* **79**, 241-263 (2013).
32. V. V. Shah, S. Goyal, H. J. Palanthandalam-Madapusi, A Possible Explanation of How High-Frequency Deep Brain Stimulation Suppresses Low-Frequency Tremors in Parkinson's Disease. *IEEE Trans Neural Syst Rehabil Eng* **25**, 2498-2508 (2017).
33. E. D'Angelo, V. Jirsa, The quest for multiscale brain modeling. *Trends Neurosci* **45**, 777-790 (2022).
34. K. Amunts *et al.*, The Human Brain Project: Creating a European Research Infrastructure to Decode the Human Brain. *Neuron* **92**, 574-581 (2016).
35. T. J. Sejnowski, The unreasonable effectiveness of deep learning in artificial intelligence. *P Natl Acad Sci USA* **117**, 30033-30038 (2020).
36. A. N. Burkitt, A review of the integrate-and-fire neuron model: II. Inhomogeneous synaptic input and network properties. *Biol Cybern* **95**, 97-112 (2006).
37. A. Falchier, S. Clavagnier, P. Barone, H. Kennedy, Anatomical evidence of multimodal integration in primate striate cortex. *J Neurosci* **22**, 5749-5759 (2002).
38. J. Du, V. Vegh, D. C. Reutens, The laminar cortex model: a new continuum cortex model incorporating laminar architecture. *PLoS Comput Biol* **8**, e1002733 (2012).
39. E. M. Izhikevich, A. Edelman, Large-scale model of mammalian thalamocortical systems. *Proc. Natl. Acad. Sci. U.S.A.* **105**, 3593-3598 (2008).
40. C. Beaulieu, M. J. J. o. C. N. Colonnier, A laminar analysis of the number of round-asymmetrical and flat-symmetrical synapses on spines, dendritic trunks, and cell bodies in area 17 of the cat. **231**, (1985).

41. J. O'Kusky, M. J. J. o. C. N. Colonnier, A laminar analysis of the number of neurons, glia, and synapses in the visual cortex (area 17) of adult macaque monkeys. **210**, (1982).
42. N. Hallonquist, Graphical Models: An Extension to Random Graphs, Trees, and Other Objects. (2017).
43. D. Kranzlmüller, P. Kacsuk, J. Dongarra, E. Gabriel, T. J. L. N. i. C. e. Woodall, Open MPI: Goals, Concept, and Design of a Next Generation MPI Implementation. **3241**, 97-104 (2004).
44. X. Du *et al.*, A Low-Latency Communication Design for Brain Simulations. **36**, 8-15 (2022).
45. W. Zhang, B. Chen, J. Feng, W. Lu, On a framework of data assimilation for neuronal networks. *arXiv preprint arXiv:2206.02986*, (2022).
46. R. Olfati-Saber, in *Decision and Control, 2007 46th IEEE Conference on*. (2008).
47. F. S. Cattivelli, A. H. Sayed, Diffusion Strategies for Distributed Kalman Filtering and Smoothing. *IEEE Transactions on Automatic Control* **55**, 2069-2084 (2010).
48. J. D. Tournier *et al.*, MRtrix3: A fast, flexible and open software framework for medical image processing and visualisation. *Neuroimage* **202**, 116137 (2019).
49. Z. Cui, S. Zhong, P. Xu, Y. He, G. Gong, PANDA: a pipeline toolbox for analyzing brain diffusion images. *Front Hum Neurosci* **7**, 42 (2013).
50. J. Veraart *et al.*, Denoising of diffusion MRI using random matrix theory. *Neuroimage* **142**, 394-406 (2016).
51. J. Veraart, E. Fieremans, D. S. Novikov, Diffusion MRI noise mapping using random matrix theory. *Magn Reson Med* **76**, 1582-1593 (2016).
52. L. Cordero-Grande, D. Christiaens, J. Hutter, A. N. Price, J. V. Hajnal, Complex diffusion-weighted image estimation via matrix recovery under general noise models. *Neuroimage* **200**, 391-404 (2019).
53. E. Kellner, B. Dhital, V. G. Kiselev, M. Reiser, Gibbs-ringing artifact removal based on local subvoxel-shifts. *Magn Reson Med* **76**, 1574-1581 (2016).
54. J. L. Andersson, S. Skare, J. Ashburner, How to correct susceptibility distortions in spin-echo echo-planar images: application to diffusion tensor imaging. *Neuroimage* **20**, 870-888 (2003).
55. J. L. R. Andersson, S. N. Sotiropoulos, An integrated approach to correction for off-resonance effects and subject movement in diffusion MR imaging. *Neuroimage* **125**, 1063-1078 (2016).
56. J. L. R. Andersson, M. S. Graham, E. Zsoldos, S. N. Sotiropoulos, Incorporating outlier detection and replacement into a non-parametric framework for movement and distortion correction of diffusion MR images. *Neuroimage* **141**, 556-572 (2016).
57. A. Leemans, D. K. Jones, The B-matrix must be rotated when correcting for subject motion in DTI data. *Magn Reson Med* **61**, 1336-1349 (2009).
58. Y. Zhang, M. Brady, S. Smith, Segmentation of brain MR images through a hidden Markov random field model and the expectation-maximization algorithm. *IEEE Trans Med Imaging* **20**, 45-57 (2001).
59. S. M. Smith *et al.*, Advances in functional and structural MR image analysis and implementation as FSL. *Neuroimage* **23 Suppl 1**, S208-219 (2004).
60. O. Esteban *et al.*, fMRIPrep: a robust preprocessing pipeline for functional MRI. *Nat Methods* **16**, 111-116 (2019).
61. S. Wang *et al.*, Evaluation of Field Map and Nonlinear Registration Methods for Correction of Susceptibility Artifacts in Diffusion MRI. *Front Neuroinform* **11**, 17 (2017).

62. J. M. Treiber *et al.*, Characterization and Correction of Geometric Distortions in 814 Diffusion Weighted Images. *PLoS One* **11**, e0152472 (2016).
63. M. Jenkinson, P. Bannister, M. Brady, S. Smith, Improved Optimization for the Robust and Accurate Linear Registration and Motion Correction of Brain Images. *NeuroImage* **17**, 825-841 (2002).
64. D. N. Greve, B. Fischl, Accurate and robust brain image alignment using boundary-based registration. *Neuroimage* **48**, 63-72 (2009).
65. R. H. R. Pruim *et al.*, ICA-AROMA: A robust ICA-based strategy for removing motion artifacts from fMRI data. *Neuroimage* **112**, 267-277 (2015).
66. W. Ding, M. K. Ng, W. Zhang, A Peaceman–Rachford Splitting Method with Monotone Plus Skew-Symmetric Splitting for Nonlinear Saddle Point Problems. *Journal of Scientific Computing* **81**, 763-788 (2019).

**Acknowledgments:** We thank Professor Trevor W. Robbins and Professor Edmund Rolls for their helpful comments on the manuscript.

**Funding:**

National Key R&D Program of China (No. 2019YFA0709502)

National Key R&D Program of China (No. 2018YFC1312904)

Shanghai Municipal Science and Technology Major Project (No. 2018SHZDZX01), ZJ Lab, and Shanghai Center for Brain Science and Brain-Inspired Technology

The 111 Project (No. B18015)

Science and Technology Innovation 2030 - Brain Science and Brain-Inspired Intelligence Project (Grant No. 2021ZD0200204)

**Author contributions:**

Conceptualization: W.L., Q.Z., J.F.

Methodology: W.L., Q.Z., J.F., DTB Consortium

Investigation: W.L., DTB Consortium

Visualization: DTB Consortium

Funding acquisition: N.X., J.F.

Project administration: Q.Z., J.F.

Writing – original draft: W.L., DTB Consortium

Writing – review & editing: W.L., Q.Z., J.F.

**Competing interests:** Authors declare that they have no competing interests.

**Data and materials availability:**

**DTB Consortium:**

Boyu Chen, Feng Chen, Siming Chen, Weiyang Ding, Xin Du, Jianfeng Feng, Zixin Gu, Mingda Ji, Chunhe Li, Yuhao Liu, Wenlian Lu, Zhihui Lv, Hengyuan Ma, Yang Qi, He Wang, Huarui Wang, Shouyan Wang, Shitong Xiang, Chao Xie, Ningsheng Xu, Leijun Ye, Longbin Zeng, Jie Zhang, Wenyong Zhang, Qibao Zheng.

**Supplementary Materials**

Materials and Methods

Supplementary Text

Supplementary Report: Simulation Report for Simulations of a Human-Brain Scaled Neuronal Network of 86 billion Neurons

Figs. S1 to S8

Tables S1 to S2

References (36–58)

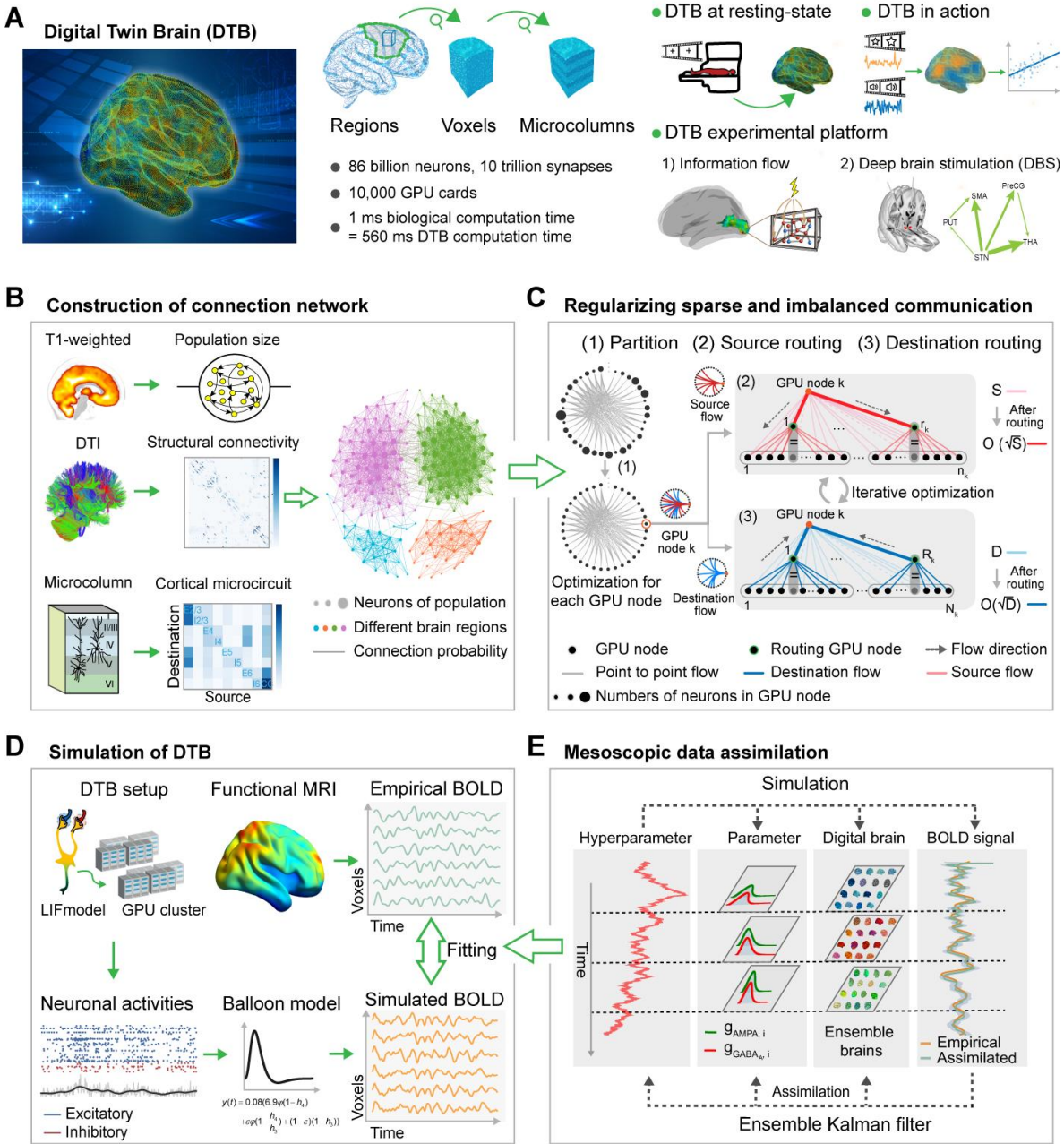


**Fig. 1. Work flow of the digital twin brain (DTB).** (A) The DTB is constructed with different numbers of spiking neurons to mimic the brain activity at three resolutions: regional, voxel and micro-column. The DTB containing 86 billion neurons and 10 trillion synapses is simulated on 10,000 GPU cards and achieved a time-to-solution of 560. Resting-state and task-based digital experiments were performed with the DTB (see Fig. 2 and 5). Besides, information flow and deep brain stimulation were also explored with the DTB (see Fig. 3 and 4). (B) Multi-modality MRI data (i.e., diffusion tensor imaging (DTI) and T1-weighted imaging) and a micro-column connection map were used to construct a probabilistic connection network. The micro-column is an elaborate network composed of six layers (L1, L2/3, L4, L5 and L6) and two types of neurons (excitatory and inhibitory neurons), whose inner connections are defined based on the neuroanatomy of the primary visual cortex of the cat. (C) An illustration for our two-level routing system, with which we could balance the data traffic and reduce the degree of graphics processing

units (GPUs) connection. **(D)** The parameter and model setting for the DTB. The Leaky Integrate-and-Fire (LIF) neuron model was used to model spike activity. Then the firing rate, obtained by counting the number of spikes of neural activity over a sliding window, is fed into the Ballon-Windkessel model to form the time series of the simulated blood oxygenation level-dependent (BOLD) signal. The synaptic conductance of AMPA and GABA<sub>A</sub> are tuned to fit the empirical BOLD signal from functional MRI (fMRI). **(E)** An illustration for our hierarchical mesoscale data assimilation method. The hierarchical brain assimilation estimated the hyperparameters by iterating two processes: simulation and filtering the hidden states by diffusion ensemble Kalman filter (EnKF). Also see Supplementary Materials for more details.

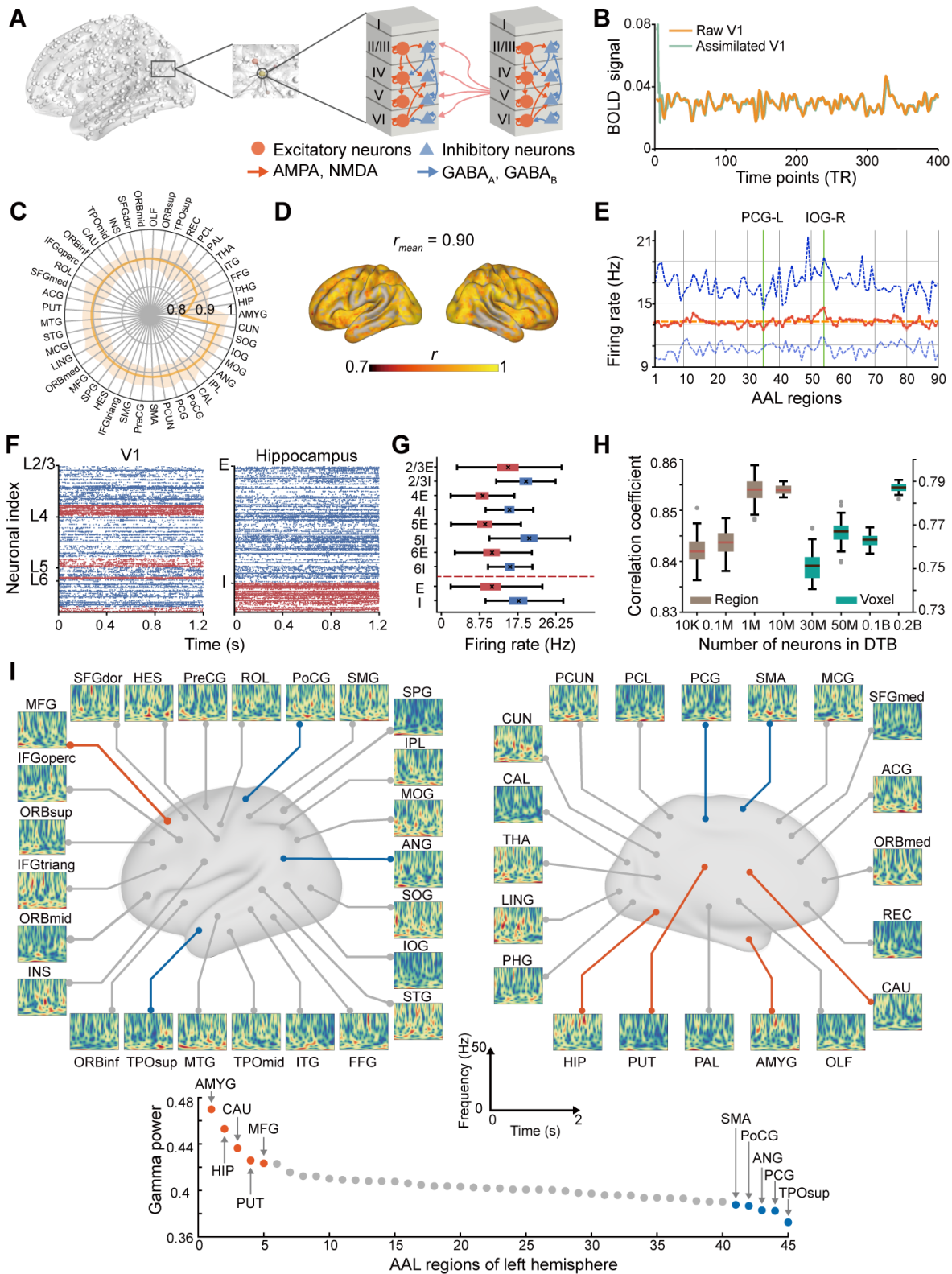


**Fig. 2. Activity of DTB in the resting state (86 B neurons, micro-column version).** (A) The sketch of the local connectivity within cortical columns in DTB. (B) An illustration of the empirical and the assimilated BOLD signals of V1 cortex. (C) Pearson correlations between the empirical and assimilated BOLD signals among micro-columns in each brain region. (D) Pearson

correlations between the empirical and assimilated BOLD signals at the whole brain cortical micro-column resolution. The yellow color represents a high correlation while black color represents a low correlation. **(E)** The overall firing rate for DTB. The bold red line represents the mean firing rate in each brain region as well as dark and light blue dashed lines represent the maximum and minimum firing rate. The green line highlights the regions with the lowest or highest mean firing rate. **(F)** Typical raster plots of spiking activity for cortical micro-columns (V1 as an example) and subcortical voxels (hippocampus as an example), respectively. Blue: excitatory neurons, red: inhibitory neurons. **(G)** Population-averaged firing rates across 21017 micro-columns and 1686 voxels. **(H)** The mean correlation between the empirical and assimilated BOLD signals among the whole brain with different numbers of neurons. **(I)** The temporal and spatial evolution of the frequency for the local field potential obtained from the DTB. Top panel: the power spectrogram of each brain region in the left hemisphere. Bottom panel: the statistic results for the power of gamma oscillation.

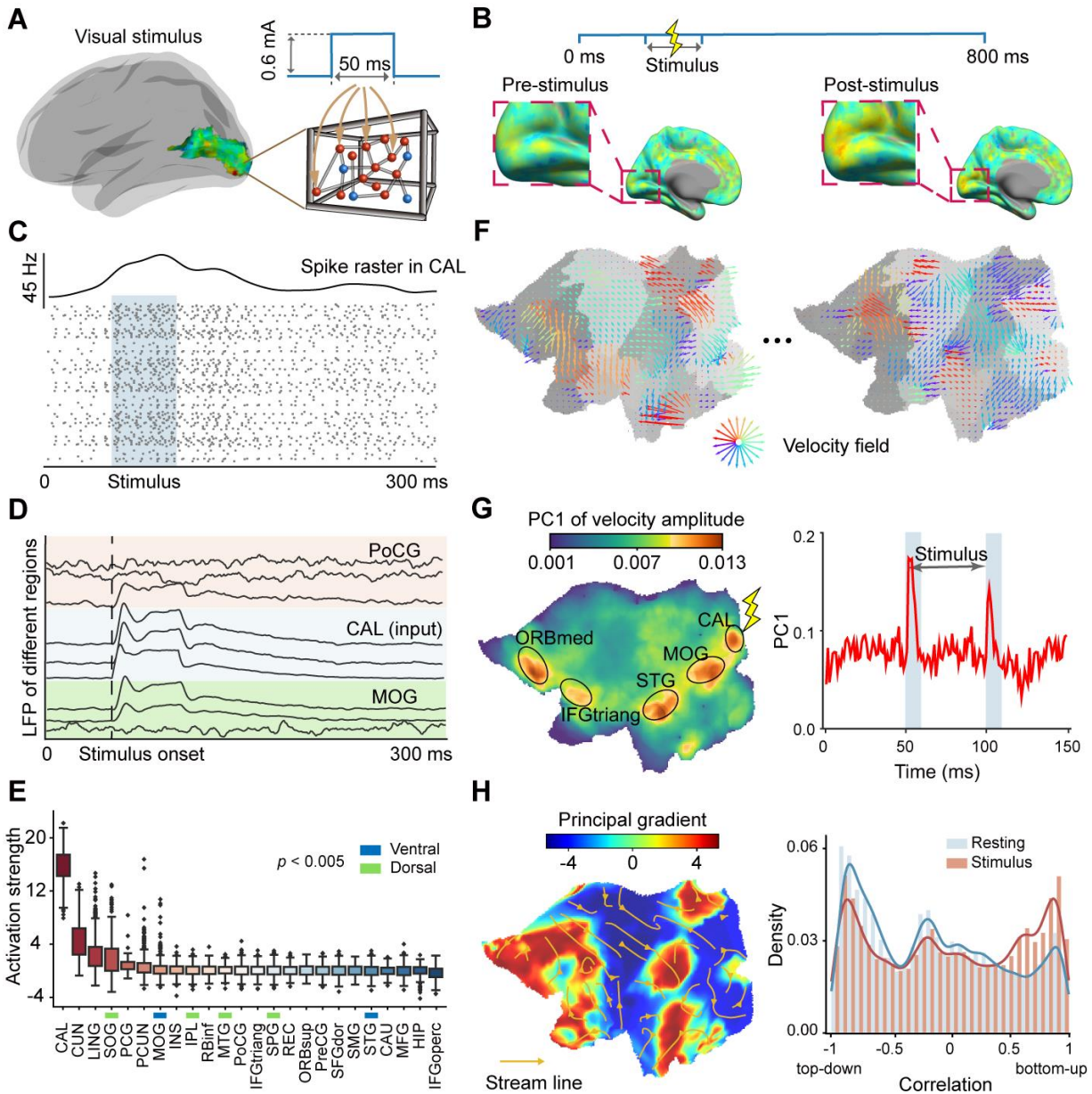


**Fig. 3. Information flow under visual stimulus in DTB (200 M neurons, micro-column version).** (A) A schematic diagram of the stimulus experiment. Pulsed electrical stimulus is applied to excitatory neurons in the primary visual cortex (Calcarine, CAL). (B) Neural activity obtained from BOLD signals before and after stimulation. (C) Spiking activity of 300 randomly sampled neurons in a voxel in CAL. The curve is the voxel-averaged firing rate. (D) The local field potential of the example brain regions during the stimulus experiment. (E) Significantly activated brain regions ordered by their activation strength in the experiment. Herein, the activation strength is defined as the integral mean value between the curves of integration value (50 ms window) over time for perturbed dynamics (post-stimulus state) compared to the basal state dynamics (pre-stimulus state) of a voxel. (F) An illustration for the spatiotemporal velocity vector field. (G) Principal component analysis for velocity amplitude. (H) The correlation between the principal gradient of fMRI and propagation direction of the velocity vector field. Also see Supplementary Material for more details.

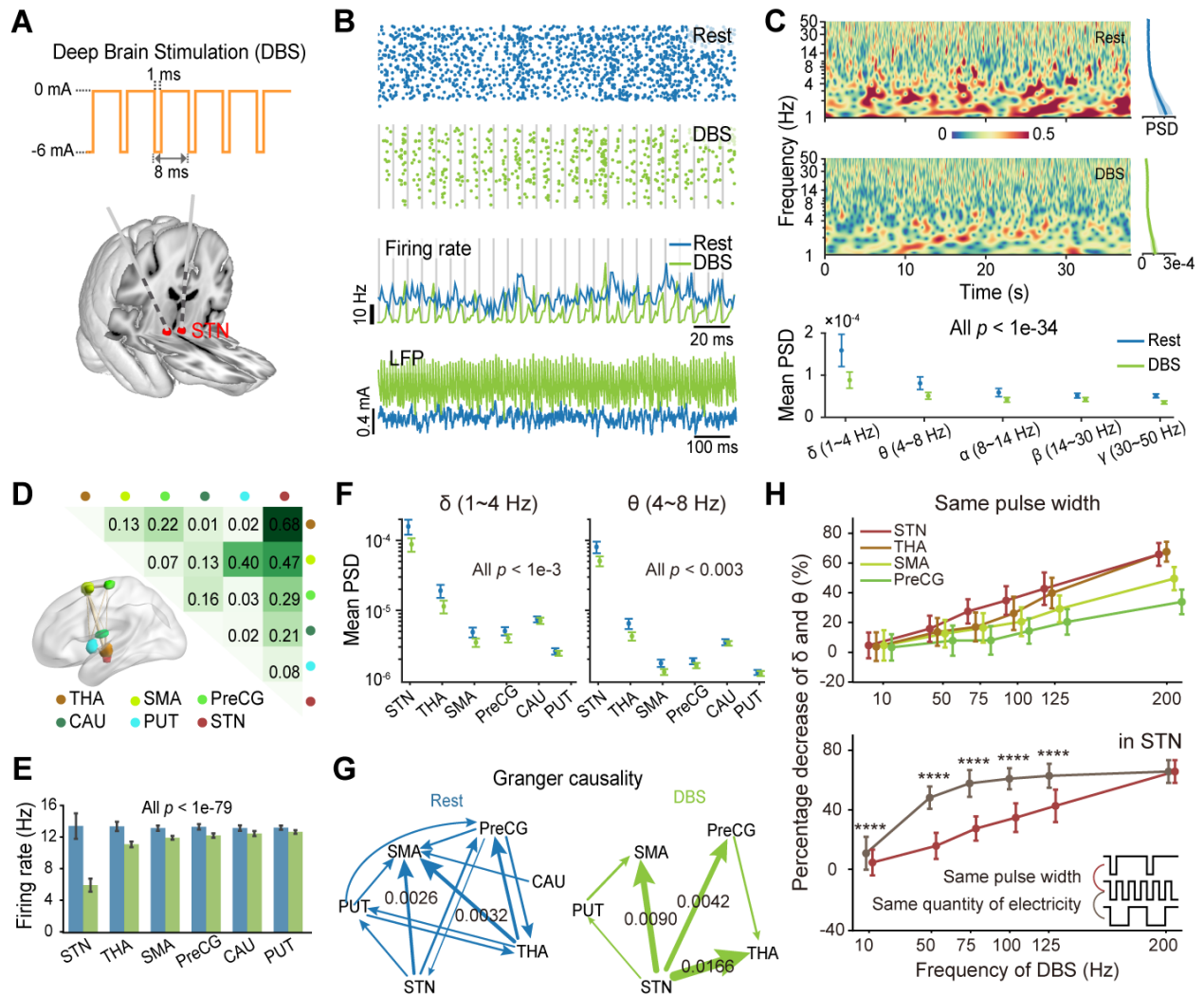


**Fig. 4. The virtual brain-computer interface (BCI) experiment on DTB (100 M neurons, voxel version).** (A) The schematic diagram of the BCI experiment. (B) The spiking activity of 500 randomly sampled neurons, the mean firing rate and the local field potential (LFP) in the left subthalamic nucleus (STN) at resting state and under the pulsed currents. (C) The time-frequency spectrum and power spectral density (PSD) of LFP in STN at resting state and DBS. (D) Five other regions of interest (ROIs) were selected to perform further analysis based on structural connectivity with STN. (E) The mean firing rate for each ROI at resting state and under the pulsed currents. (F) The mean PSD of the low-frequency oscillation (i.e., delta and theta oscillation) for each ROI at resting state and under the pulsed currents. (G) The Granger causality among the above six ROIs at resting-state and under the pulsed currents. (H) The outcomes of the different pulsed current settings, i.e., with the same pulse width and with the same quantity of electricity, respectively.

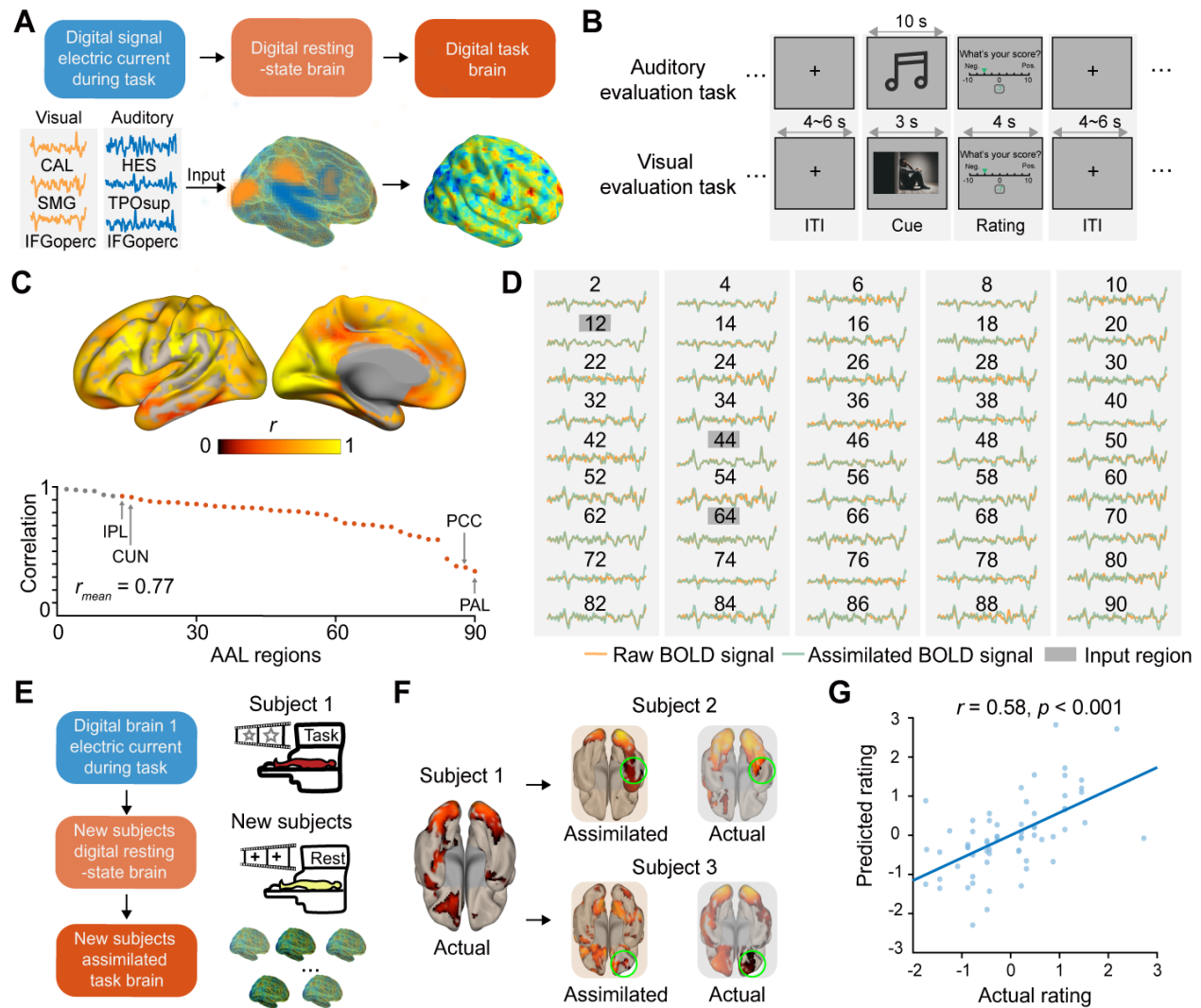


**Fig. 5. DTB in action (100 M neurons, voxel version).** (A) Workflow for the DTB in action. We firstly simulate the BOLD signals of the reference brain regions to obtain electric input currents. Then we injected the above currents into the DTB to yield the digital task brain. (B) A schematic illustration of the auditory and visual evaluation task. (C) Pearson correlations between the empirical and assimilated BOLD signals at both voxel- and region-level. (D) The illustrations of the empirical and the assimilated BOLD signals with a time lag of 4 for each region in right hemisphere during the visual evaluation task. (E) A schematic illustration of the digital brain virtual experiment, in which we injected current during the task from subject 1 into the digital resting state brain of other subjects, to yield a digital task brain of other subjects. (F) The activation patterns of the assimilated digital task brain and its corresponding biological brain. (G) The predicted performance based on the assimilated DTB of the visual evaluation task. Also see fig. S8 for the auditory evaluation task and Supplementary Materials for more details.

## Supplementary Materials

### Materials and Methods:

#### *The digital twin brain (DTB)*

The whole brain neuronal network model presents the computational basis of the Digital twin brain and is composed of two components: the basic computing units and the network structure. The basic computing units of the DTB are neurons and synapses, and the spike signal transmitted between neurons by synapses are action potentials, i.e., spikes. Each neuron model receives the postsynaptic currents as the input and describes the generating scheme of the time points of the action potentials as the output. The synapses have different models due to the diverse neurotransmitter receptors. The computational neuron is an integral unit of the received presynaptic spikes from synapses as the input and generates spike trains as the output postsynaptic currents. The network model gives the synaptic interactions between neurons by a directed multiplex graph. Structural MRI images (i.e., T1 weighted data and diffusion weighted data) from biological brains are used to indirectly and partially measure the proportions of grey matters (neurons) in subregions and neuron axions between sub-regions

#### *Spiking neurons and synapses model*

The computational neuron model is generally a nonlinear operator from a set of input synaptic spike trains to an output axon spike train, described by three components: the subthreshold equation of the membrane potential that describes the transformation from the synaptic currents of diverse synapses; the synaptic current equation describes the transformation from the input spike trains to the corresponding synaptic currents; the threshold scheme gives the condition for triggering a spike by membrane potential value. Herein, the configuration can be sufficiently general to include diverse spike neuron models of single or multi-compartments that transfer spike trains of action potentials as the signals.

Let  $I_{i,syn,u}(t)$  stand for the synaptic current at the synapse type  $u$  of neuron  $i$  and  $T_i = \{t_1^i, t_2^i, \dots, t_n^i, \dots\}$  where  $t_n^i$  is the time point of the  $n$ -th spike of neuron  $i$ , or equivalently  $N_i(t)$  stands for the count of spikes of neuron  $i$  before  $t$ . A computational neuron is a nonlinear mapping from the synaptic current  $\{I_{i,syn,u}(t): u, t\}$  to the spike train  $T_i$ :

$$T_i = SpN[\{I_{i,syn,u}(t): u, t\}]$$

Herein, we consider the leaky integrate-and-fire (LIF) model as neuron (36). A capacitance-voltage (CV) equation describes the membrane potential of neuron  $i$ ,  $V_i$ , when it is less than a given voltage threshold  $V_{th,i}$

$$C_i \dot{V}_i = -g_{L,i}(V_i - V_L) + \sum_u I_{syn,i} + I_{ext,i}, V_i < V_{th,i} \quad (1)$$

Here  $C_i$  is the capacitance of the neuron membrane,  $g_{L,i}$  is the leakage conductance,  $V_L$  is leakage voltage and  $I_{ext,i}$  is the external stimulus. When  $V_i = V_{th,i}$  at  $t = t_n^i$ , neuron registers a spike at time point  $t_n^i$  and the membrane potential is reset at  $V_{rest}$  during a refractory period

$$V_i(t) = V_{rest}, \quad t \in [t_k^i, t_k^i + T_{ref}] \quad (2)$$

After then,  $V_i$  is governed by CV equation (1) again.

The synapse model presents a nonlinear mapping from the spike trains of the presynaptic neuron to the postsynaptic current:

$$I_{i,syn,u} = Syn_u[\{T_j: j \rightarrow i\}]$$

Here,  $j \rightarrow i$  stands for the case that neuron  $j$  is synaptically connected to neuron  $i$ . We consider an exponential temporal convolution for this:

$$\begin{aligned} I_{u,i} &= g_{u,i}(V_u - V_i)J_{u,i} \\ J_{u,i} &= -\frac{J_{u,i}}{\tau_i^u} + \sum_{k,j} w_{ij}^u \delta(t - t_k^j) \end{aligned} \quad (3)$$

Here,  $g_{u,i}$  is the conductance of synapse type  $u$  of neuron  $i$ ,  $V_u$  is the voltage of synapse type  $u$ ,  $\tau_i^u$  is the time-scale constants of synapse type  $u$  of neuron  $i$ ,  $w_{ij}^u$  is the connection weights from neuron  $j$  to  $i$  of synapse type  $u$ ,  $\delta(\cdot)$  is the Dirac-delta function and  $t_k^j$  is the time point of the  $k$ -th spike of neuron  $j$ . Herein, we consider at least four synapse types: AMPA, NMDA, GABA<sub>A</sub> and GABA<sub>B</sub>.

#### *Cortex voxel laminar model*

We consider the laminar model that was established based on the neuroanatomy of the primary visual cortex of the cat (15,37), which was widely used to build up large-scale neuromorphic computational models (38, 39). In this model, the cortex is composed of six layers: L1, L2/3, L4, L5 and L6, equipped with excitatory and inhibitory neurons. At each layer, the number of neurons is proportional to the statistics given in Du. *et al* (38), which originated from Binzegger. *et al* (15). Early studies with physiological experiments in area 17 of cats (40) and adult macaques (41) showed consistent results on the synaptic distribution of excitatory and inhibitory neurons in each layer (15). We follow the data of assigned synapses. To treat the sources of the unassigned synapses, based on these previous works (15, 39), we made modifications to the data given the following assumptions: 1) all of the unassigned symmetric (i.e., inhibitory) synapses in layer 1-6 originate from smooth (inhibitory) neurons in the layer where the synapses are located (15); 2) 95% of the unsigned asymmetric (i.e., excitatory) synapses come from other cortical regions (39). Hence, we derived the laminar connections (table S1).

It should be highlighted that L1 contains synapses onto the apical dendrites of neurons in lower layers (15, 37). The numbers of the input synapses to each layer in the voxel coming from other layers and other cortical region are proportional to the statistics given in Du. *et al* (38) as well. These actual numbers of input synapses of each layer can be calculated by fixing the average number of input synapses of neurons in this voxel constant. We set that the output synapses all come from the excitatory neurons in L5.

#### *Structural MRI based whole-brain structural network model*

The network architecture of this computational model can be arbitrary including feedforward and recurrent. Herein, we consider a general network model of the human or animal brain for simulation and data simulation, inspired by structural imaging data. Due to the resolution scale of brain structural data, structural information of resolution higher than the imaging technique can never be seen, and so we propose a network model of hierarchical random graph with constraints and multiple edges (HRGCME), to represent the neuron pairwise synaptic connections.

The HRGME model is a set of weighted directed graphs with hierarchical structures.  $\mathcal{G} = \{G^p: p = 1, \dots, P\}$ , where  $G^p = (V^p, E^p)$  with node set  $V^p = \{v_j^p\}$ , edge set  $E^p$ , the corresponding adjacency matrix  $W^p = \{w_{ij}^p: i, j \in V^p\}$  and node attributes  $A^p = (A_i^p: i \in V^p)$ . In the following,  $|A|$  denotes the cardinal dimension of the set  $A$  of finite elements. For each  $p > p'$ , graph  $G^p$  can be regarded as composed of the nodes and edges from  $G^{p'}$ , where  $|V^p| \leq |V^{p'}|$  naturally holds. In detail, there exists a disjoint splitting of the node sets  $V^{p'}$ ,  $\{C_l^{p,p'}: l = 1, \dots, |V^{p'}|\}$ , namely satisfying 1)  $C_l^{p,p'} \subseteq V^{p'}$ ; 2)  $C_{l_1}^{p,p'} \cap C_{l_2}^{p,p'} = \emptyset$ ; 3)  $\cup_l C_l^{p,p'} = V^{p'}$ . Each node of  $V^p$  define one node set  $\{C_l^{p,p'}: l = 1, \dots, |V^{p'}|\}$ , such that 1)  $(v_{j_1}^p, v_{j_2}^p) \in E^p$  only if there exists  $(v_{q_1}^{p'}, v_{q_2}^{p'}) \in E^{p'}$  with  $v_{q_1}^{p'} \in C_{j_1}^{p,p'}$  and  $v_{q_2}^{p'} \in C_{j_2}^{p,p'}$  and 2)  $|w_{j_1 j_2}^p|$  is proportional to  $\sum_{v_{q_1}^{p'} \in C_{j_1}^{p,p'}, v_{q_2}^{p'} \in C_{j_2}^{p,p'}} |w_{q_1 q_2}^{p'}|$ . Here,  $p$  stands for the order of hierarchy that indicate the resolution scale of the obtained data or knowledge and  $p = 1$  stands for the scale of neurons. A large  $p > 1$  can stand for the scale of lower resolution scale, for instance,  $p = 2, 3, 4$  are corresponding to a micro-column, voxel, region of interest (ROI) respectively. Each type of synaptic connection is represented by a graph set  $\mathcal{G}^u$ , which compose a multiplex network by the way that all  $\mathcal{G}^u$  share the same node sets. The setup of hierarchies is determined by the structure data and/or knowledge.

We illustrate this model by the data of MRI brain scanning and the knowledge of the laminar structure of the primary visual cortex of cat. We define  $\mathcal{G}^u = \{G^{u,p}: p = 1, 2, 3\}$ ,  $u = \text{AMPA, NMDA, GABAa, GABAb}$ , with  $G^{u,p} = (V^p, E^{u,p})$  where  $p = 1$  stands for neuronal network such that  $V^1$  is the neuron set. There are two types of neurons: excitatory (pyramidal) neurons and inhibitory (inter) neurons. It should be highlighted that edge of  $E^{u,p}$  with  $u = \text{AMPA, NMDA}$  occurs only from excitatory neuron to other neurons and edge of  $E^{u,p}$  with  $u = \text{GABAa, GABAb}$  occurs only from inhibitory neuron to other neurons. We do not allow self-loop and multiple connection for a pair of neurons on graph  $G^{u,1}$ . For the above settings mentioned, we can rewrite it formally: 1)  $G^{u,1}$  share the same node sets for all  $u$ , 2) graph of type AMPA and type NMDA have the same edges and the same for inhibitory type. 3) the corresponding weight of graph for different synaptic types are different but obey the same distribution (uniform distribution  $U[0, 1]$  in our model). And  $p = 3$  stands for a network of voxels, where  $V^3$  is the set of voxels,  $|C_l^{3,1}|$  proportional to the gray volume of voxel  $l$  measured by the voxel-based morphometry (VBM), and the element  $w_{ij}^{\text{AMPA},3}$  and  $w_{ij}^{\text{NMDA},3}$  of  $W^{\text{AMPA},3}$  takes values of the fibre counts between voxel pair  $(i, j)$  obtained from DTI. The ratio of the number of excitatory neurons over that of inhibitory neurons of each voxel was set as 4:1. The ratios between the number of excitatory synaptic (out-) edges within each voxel, that of excitatory synaptic (in-) edges from out of this voxel, and that of the inhibitory synaptic edges (within the voxel) are constant as 5:3:2. As for  $p = 2$ , each cortical voxel is regarded as a micro-column of six laminar layers with eight disjoint splitting populations (layer 2 and layer 3 merge to L2/3 and no L1, each layer splits 2 populations, Exc. and Inh.):  $C_l^{2,1}$ ,  $l = j_1, \dots, j_8$ . Each  $|C_l^{2,1}|$  is proportional to  $|C_j^{3,1}| * T_l * D_l$ , where  $T_l$  stands for the thickness of layer where population  $l$  resides and  $D_l$  stands for the neuronal density of population  $l$ . For each non-cortical voxel  $v_j^3$ , we do not consider its further structure and regard it as a canonical voxel structure which contains 2 sets of excitatory and inhibitory neurons ( $C_E^{2,1}: C_I^{2,1} = 4: 1$ ). To be consistent with the above setting, the connections between populations (long-range

connections) are all excitatory connections, it equally says that both  $E^{u,2}$  and  $W^{u,2}$  as empty sets when  $u \neq \text{AMPA, NMDA}$ .

### Network topology implementation

Based on the HRGCME proposed above, we are now ready to construct the DTB. The DTB provides three resolution scales of network models, namely a brain region version, voxel version, and micro-column version, which corresponds to  $\mathcal{G}^{1,4}$ ,  $\mathcal{G}^{1,3}$ ,  $\mathcal{G}^{1,2}$ , respectively. We use the micro-column version as an example to implement this network model. For the graph set  $\mathcal{G}^{1,2}$ , we need to construct the graph  $G^2$  firstly and then convert to  $G^1$  with the predefined network size and in-degree scale. In detail, we begin from computing the node attributes which represents the scale of population size. Formally, we use  $S = [S_m]$  to stand for VBM vector for brain regions (voxels),  $T = [T_i]$  and  $D = [D_i]$  for thickness vector and neuronal density vector respectively in a micro-column. Then we can easily derive the node attribute of  $G^2$  as

$$A(i) = \begin{cases} \frac{S_m}{\sum S_j} \times \frac{T_i}{\sum T_i} \times D_i & i \in C_m^{2,3} \text{ and } |C_m^{2,3}| = 10 \\ \frac{S_m}{\sum S_j} \times (0.8 \text{ or } 0.2) & i \in C_m^{2,3} \text{ and } |C_m^{2,3}| = 2 \end{cases} \quad (4)$$

Here,  $|C_m^{2,3}| = 10$  implies a cortex voxel with laminar model and  $|C_m^{2,3}| = 2$  implies a non-cortex voxel, where multiplied with 0.8 standing for excitatory neuron. and 0.2 for inhibitory neurons. Therein, we assign the neuronal size of population  $i$  as  $N_i = A(i) * |V_1|$ . Secondly, the connection matrix of  $G^2$  is derived by applying the kronecker product of the normalized DTI matrix (voxel level) and micro-circuit matrix  $M$  (table S1) as

$$p(i \leftarrow j) = \{DTI \otimes M\}_{i,j} \quad (5)$$

where  $i, j$  represents index of population respectively and  $p$  denotes the derived connection probability. Thirdly, we fix the average number of input-synapses of neuron in this voxel to  $\bar{d}$  and then calculate the actual number of input synapses for neurons of each population as:

$$d(i \leftarrow \cdot) = \frac{\bar{d} \times N(i)}{\sum N(j)} \times \frac{\sum_j M_{i,j}}{\sum_{i,j} M_{i,j}}, \quad \text{where } i, j \in C_l^{2,3} \quad (6)$$

In this work, we set the source of cortico-cortical connection to be L5E and the destinations are distributed in the 2/3, 4, 5 and 6 layers. According to equation (5) and equation (6), the in-degree of population  $i$  from population  $j$  is calculated as:

$$N_{\text{syn}}(i \leftarrow j) = d(i \leftarrow \cdot) \times p(i \leftarrow j) \quad (7)$$

In summary, we implement this network model based on an extension of  $k$ -random graph (42). Firstly, we set the number of neurons per population as equation (4). Secondly, for each neuron, according to its property (excitation or inhibitory neuron) and location (the voxel and/or layer if in a cortical voxel), we can calculate the number of synaptic links from each neuron population (the non-cortical voxel or the layer of the cortical voxel) defined in  $G^{1,2}$  to this given neuron (Eqs. 5-7). Thirdly, we select each source neuron in that neuron population by equal probability without replacement iteratively.

In the present paper, we set  $\bar{d} = 100$ , despite of generally the average synaptic number of each neuron varying from  $10^3$  to  $10^5$  due to the limit of the communication and memory

bandwidths. Since the main simulation cost comes from communicating and reading spikes between neurons, as detailed in the following section, it cannot be afforded with a large synaptic degree for a whole-brain-scale neuronal network simulation by our GPU-based high-performance computer (HPC).

### *Whole brain simulation on GPUs*

We implement the computation of simulating the neuronal network with the computational neuron model and synaptic network model by GPUs (clusters), due to their power of parallel computation. The simulation of the neuronal network is composed of two components: the spike integral that integrates the synaptic input spike trains to the membrane potential, which is set as an individual module/class and hence is flexible to different neuronal model; and the spike communication that transfers spike trains between neurons. There are two different types of neuromorphic computation methods available in this simulation. For the first synchronous method, the subthreshold evolution, the spike triggering judgement and the transferring of spikes are executed with the uniform time step length (1 ms) and thus the spikes are coded in a binary way, i.e., 1 and 0 stand for “spike” and “no-spike” respectively at the time bin, for communication. For the second asynchronous method, the membrane potential of each neuron is integrated from the input spike trains independently until the output spike is triggered or it reaches the upper bound of time interval (5 ms), and the spike is coded with its time stamp within the time interval (5 ms) for communication. The former is a general and direct calculation method, of which the simulation accuracy can be verified by comparison with the local CPU simulation of sampling some neurons. However, the latter has higher computational efficiency but cannot verify the accuracy of the simulation results. Therefore, after comprehensive consideration, DTB adopts the synchronization algorithm as the operation mechanism in the whole calculation process.

### *Push-based spike integrals*

We use synchronous push-based spike integrals to numerically evolve the membrane potentials of each neuron at the incoming synaptic spikes from other neurons. The push-based spike integral is a synchronous method to integrate the membrane potential on the subject neuron by summing up the integrals of all spikes (the postsynaptic currents, Eq. 3) that are sent to this neuron in the given time bin. The Euler iteration method of Eqs. (1-3) are formulated as follows with  $\Delta t = 1 \text{ ms}$ :

$$\left\{ \begin{array}{l} J_{u,i}(t + \Delta t) = \exp\left(-\frac{\Delta t}{\tau_i^u}\right) J_{u,i}(t) + \sum_j w_{ij}^u A_j(t) \\ V_i(t + \Delta t) = V_i(t) + \sum_u \Delta t J_{u,i}(t + \Delta t) g_{u,i}(V^u - V_i(t)), \\ V_i(t + \Delta t) = V_{rst}, \text{ when } t + \Delta t \in [t_k^i, t_k^i + T_{ref}] \end{array} \right. \quad (8)$$

where  $A_j(t)$  is the spike label of the neuron  $j$  in the last time bin  $[t - \Delta t, t)$ ,  $A_j(t) \in \{0, 1\}$ . Since the spikes of each neuron are sparse in total, we use the following spike-driven scheme as follows:

---

**Algorithm 1** push-based spike integrals

---

**Input :**

All parameters of neurons and graph structure;

**Output :**

Membrane potentials and spike trains of all neurons;

- 1: For any neuron, update neuronal state  $A_j(t)$ ;
  - 2: search spiking neurons, and stack them as *SpikeList*;
  - 3: **for**  $i \in \text{SpikeList}$  **do**
  - 4:     update upcoming synaptic inputs to post-synaptical neurons.
  - 5:     determine firing neurons and reset to  $V_r$  within a refractory time.
  - 6: **end for**
- 

As shown in Algorithm 1, the spike is coded as  $A_j(t)$  in this method. A destination-address list is stored for each neuron. When a spike is registered by neuron  $j$  at time  $t$ , i.e.,  $A_j(t) = 1$ , neuron  $j$  sends this spike package to all other neurons connected from  $j$  following its DST-address list, which triggers spike operation at all connected neurons. Although it may cost additional time on atom operations, it is still much faster than the natural pull-based algorithm in practice because it takes full advantage of both the sparsity of  $A_j(t)$  and  $w_{ij}^u$ .

To initialize the spike trains and avoid synchronization of neuronal spikes, noting that we initially set the homogeneous values for each type of parameters and the identical initial values for Eq. 1, we inject a background spike into the output spike train of each neuron with a low independent identical probability from 0.5% to 1%, turning out an external spike frequency from 10-20 Hz.

*Communication of synaptic spikes*

The major cost of the DTB simulation lies on the spike communication between neurons. Details can be referred to (9). In the DTB, we use the existing techniques and protocols of high-performance computer (HPC) of GPU clusters and map the synaptic spike transmission on them. The basic assembly of neurons is according to the GPU card where the neurons are assigned for computation. It can contain a part of a neuronal network and multiple networks when conducting simulation. Because the computing device (GPU) is known where each spike communication occurs, we do not need to take the GPU label into consideration when labelling the neurons. The neurons and their synapses at each GPU are coded in a single link table (fig. S1), including: 1) the attributes (parameters) of each neuron, which are used to evolve its membrane potential; 2) The attributes of each incoming synapse, composed of the label of neurons coming from (4 bytes for neuron index and 2 bytes for block index) and going to (4 bytes), and the type of synapse (1 byte) and its synaptic weights. We do not contain the outward synapses of this block into the link table. By this way, we use 11 bytes (4+2+4+1) to encode each synapse (except the connection weight) and highlight that this bit size per synapse is totally independent of the scalability of the neuronal network of the DTB but only depends on the number of neurons assigned to a single GPU.

Thus, each spike is encoded only by the label of its source neuron (without the block/GPU label). The GPUs are initialized by handshakes to know the labels and the Message Packet Interface (MPI) rank of the GPUs by sharing their link tables once for all. At each time bin, the GPU bags the spikes that are generated by the neurons on this GPU and then send them off. When a GPU receives a bag of spikes, the label of the source neuron encoded in the spike and

the synapse label queried from the link label can be obtained, and neurons in this GPU can update their states by calculating the accumulative spike integrals.

The physical and data-link transmission of synaptic spikes is implemented by the communication interface and equipment of the GPU cluster of three layers: The VRAM on the GPU can communicate the synaptic spikes of neurons within the block; the PCIe and shared memory on CPU with communication between GPUs on the same cluster node; the InfiniBand (IB) switcher conducts the communication between cluster nodes (fig. S1).

We implement the synaptic spike communication by the Open MPI (43). When implementing a large-scale neuronal network which cannot be assigned on a single GPU and even a single cluster node, we reduce the communication traffic by two directions. On the one hand, optimizing the layout of neurons on GPUs. We make synaptic communication as much as possible firstly in the same GPU or secondly in the same node. On the other hand, based on communication efficiency of the communication interfaces, we optimize the routines between nodes in the IB switchers according to the real-time communication traffics.

#### *Voxel-GPU mapping, topology and routing*

To achieve the data traffic management problem, we presented an optimization framework to improve the delivery of hyper-giant traffic in brain simulations, leveraging the re-configurability along three dimensions: voxel-GPU mapping, topology and routing. We employ a low-latency communication design method to optimize the efficiency to simulate the whole-brain neuronal model on GPUs with Open-MPI (44).

We focused on the flow of logical data in a HPC composed of GPU nodes. Since the physical network architecture cannot be changed, when designing routing for a system, we are to consider some limitations including hardware conditions (such as bandwidth limitations) and frameworks on HPCs.

Both the partition algorithm and routing method need to consider balancing the data traffic among GPUs (fig. S2). Owing to the limitations of hardware and the different connected relationships between neurons, planning the partitioning of neurons into different GPUs and designing the routing of the communication between these GPUs can increase hardware utilization and connect more of the information between neurons in the same GPU. Furthermore, the number of connections across different GPUs is reduced to minimize the connections of the entire network. An increased number of connections across different GPUs will result in memory overhead in the network, causing time delay and affecting even the normal operation of the system. When the number of connections is smaller, the system will incur fewer overheads, while performing the task.

During the development process for communications, limitations including hardware conditions (such as bandwidth limitations) and frameworks on HPCs being difficult to change, should be considered. Additionally, when designing routing for a system, each additional layer of routing increases the waiting time of the hardware. The number of layers in such a routing is inversely proportional to the number of connections between different GPUs, requiring tradeoffs for specific scenarios.

Using the partitioning algorithm, we may assign neurons to GPUs in the system based on the amount of data with which they interact. However, owing to the difference in the amount of data information contained by the neurons, differences still exist in the amount of data between different GPUs. Without proper traffic processing, thousands of GPUs in a HPC that are used

to simulate the human brain will communicate with each other simultaneously, which will inevitably lead to network congestion. The GPUs all need to communicate with a GPU at the same moment (fig. S3), if the amount of data generated by one GPU in the simulation process is more than that generated by other GPUs for the total system running time, the result can only be obtained after all GPUs have fully executed. That is, when the system is running, the resources of the majority of GPUs are wasted, which is not conducive to minimizing the running time of the entire system. Thus, balancing the amount of data generated in each GPU as far as possible can promote the improvement of the low-latency communication design in brain simulations. Furthermore, as the simulation is run on the HPC, communications among a large group of GPUs only adopt the functions in the MPI architecture; therefore, to control the data traffic, logical hierarchical processing must be performed between the GPUs. The two-level routing proposed in this paper is used to balance the communication speed and degree of congestion between GPUs. The routing for data traffic in brain simulation here is set to two levels; that is, communication between any two GPUs can only be forwarded at most once. Such a structural design satisfies all the restrictions mentioned above as much as possible, while balancing the number of connections and forwarding time between GPUs and the traffic between all GPUs in the system as much as possible. The GPUs in the system are divided into groups according to the amount of data that can be communicated between GPUs. The amount of data that need to be exchanged between the GPUs in the same group is relatively large, and the amount of data exchanged between the GPUs in different groups should be as little as possible. GPUs in the same group communicate with each other through direct connections, and GPUs in different groups need to identify the corresponding GPU node in their group to forward data traffic.

While a GPU wants to connect to a GPU in another group, the GPU needs to judge whether it can communicate with it on behalf of its group. If the answer is no, it needs to find another GPU as the bridge node to transmit its information. The amount of data that needs to be exchanged between the GPUs in the same group is relatively large, and the amount of data exchanged between the GPUs in different groups should be as little as possible. The reason is that GPUs in the same group communicate with each other through direct connections, and GPUs in different groups need to identify the corresponding GPU node in their group to forward data traffic. Moreover, a group of GPUs on the same switch in the physical structure speeds the information interaction. In addition, because each connection requires a thread to be started, the time taken to start the thread in the whole system can be reduced by reducing the number of connections. By matrix reordering, GPUs with dense connections or no connections can be grouped together to reduce the number of connections (fig. S4).

#### *Parameter initialization*

We initialize parameters according to the spike dynamics of networks in the resting state (without specifically external inputs) numerically, according to the following aspects: 1) Distribution of the firing rates with respect to neurons; 2) Response map of firing rate with respect to the synaptic conductance parameters; 3) asynchronization between neuron spike trains. The first item is to guarantee biologically sound spiking dynamic behaviours, the second is to guarantee that the spike dynamical behaviours are mainly generated and maintained not by injected spike noises but the network structure, and furthermore, the third is to guarantee that it is not the initial homogeneous parameter but the heterogeneity of the network structure accounts for the neuronal spiking dynamics.

We utilize an approximate off-network method to initialize the parameters (i.e., the conductance parameters) to enable the network to simulate spike trains of a stable frequency and normal variance, for on-network simulation costs much. Given the large-scale network configuration, we extract the smallest unit that can characterize the network infrastructure. In this case, the entire network can be expressed as a complex coupling of such units (such as a single neuron in a sparse network, micro-column in a cortical laminar network). Consider a small network with some such units, our goal is to find a stable parameter so that enable the unit can fire with the same frequency in the network under a given spike input. We inject statistically independent Poissonian spike trains with a fixed frequency (5-10 Hz) to each unit and adopt a semi-automatic iterative method to update the synaptic conductance parameters until all selected neurons stably fire with the same frequency (10-20 Hz) or up to a limit iteration (we set 20 herein). From the iteration process, we can see that the off-line network gradually approaches the firing state specified by us, and in which parameters can converge in about ten iterations (fig. S5). At last, the derived parameters are set in the large scale network simulation. It has been seen by the network simulation that the output spike trains are approximately stable at the given frequency.

In detail, for a given large-scale network model, we aim to find a set of proper parameters (explicitly, conductance parameters of synapses  $g_{ui}$ ) for the spike network to maintain a stable firing rate. To do this, we reduce the network size while maintaining consistent topology and neuron properties, and adopt the semi-automatic iterative method in the off-line network to update the parameters, until the network converges.

Reviewing the CV equations (Eq. 1), the membrane potential is modulated by 4 synaptic currents and the leaky current:

$$C\dot{V} = I_{leaky} + I_{AMPA} + I_{NMPA} + I_{GABAa} + I_{GABAb} \quad (9)$$

where  $I_{leaky} = -g_{leaky}(V - V_{leaky})$  depends on the membrane potential and can be approximated as  $I_{leaky} = -g_{leaky}(\frac{V_{th} + V_{rest}}{2} - V_{leaky})$  in the evolution process. So, given the allowed maximum fire rate of the network, we can calculate the EPSP  $I_{exc}$  for the consideration that the network fires at a maximum level if the inhibitory synaptic current is zero. Then we can calculate the IPSP  $I_{inhi}$  while the network fires at a stable firing rate  $\Gamma_{normal}$ . Empirically, in order to prevent the network collectively oscillating, we set the ratio of the 2 excitatory synaptic currents to be 0.3 and 0.7 respectively (reducing the ratio of excitatory current of fast channels). The ratio of the two inhibitory channels is set to 0.5 and 0.5. Now, we can compute the synaptic current for 4 chemical channels respectively according to the EPSP and IPSP. Empirically, the synaptic currents are approximately linear in relation to synaptic conductance, so we can tune parameter  $g_{ui}$  to enable the synaptic current close to the PSPs value that we calculate above. The detailed algorithm is as follows:

---

**Algorithm 2** Parameter Initialization

---

**Input :**

Default fire rate:  $r_{normal}$ ;  
Maximum fire rate:  $r_{max}$ ;  
Channel noise rate:  $r_{input}$ ;  
Iteration:  $N$ ;

**Output :**

Conductance coefficients:  $g_u$ ;

- 1: Caculate appropriate PSPs:  $I_u$ ;
  - 2: Initialize the coefficient:  $g_u^0$ ;
  - 3: Set  $i = 1$ ;
  - 4: **while**  $i < N$  or  $\bar{I}_u \approx I_u$  **do**
  - 5:     run the off-line model
  - 6:     obtain the temporary synaptic current:  $\bar{I}_u$
  - 7:     modify  $g_u^i = g_u^{i-1} \times I_u / \bar{I}_u$
  - 8: **end while**
- 

In both brain sparse network and voxel laminar model, we use the semi-automatic iterative method to initialize the conductance coefficients of synapses for a nontrivial state. Specifically, in the model at the brain region version and the voxel version, we generate a 2000 neuron small off-line network, while keeping the in-degree 100 for all neurons. In the laminar model (cortical column version), we think of the voxel structure of eight populations as a unit, in which the cortico-cortical connection is fed back to the voxel from L5. Then the in-line simulation of real network utilizing the method as above is run to initialize the parameters and validate their effectiveness.

***Bayesian inference framework***

The details of the inference approach can be referred to (45). Generally speaking, let  $x(t)$  be the neural activity (series) of the brain and the dynamical system model of neuronal network be formulated as follows

$$\dot{x} = f(x, \theta)$$

where  $\theta$  stands for the parameters in the model. Let  $y_t = h[x_t]$  be the observation (series) of the neural activity. The basic Bayesian inference becomes

$$P(\theta|y_t) \propto \int P(y_t|x_t, \theta)P(x_t|\theta)P(\theta) d[x_t] \quad (10)$$

where  $d[x_t]$  denotes the path integration since  $x_t$  is sequential data, rather than over state/observation points.

Eq. 1 implies that the number of parameters involved in the neuronal network model is possibly much larger than the number of data points, even higher in order of magnitude, due to the low resolution of the data in both space and time scales, for example the fMRI scanning data. So, it is always overdetermined if conducting this sort of Bayesian inference. Alternatively, we establish a hierarchical Bayesian inference by introducing hyper-parameter  $\vartheta$  to describe the distribution of parameters (fig. S5), which may contain the important neurophysiological information of these parameters. Then, Eq. 10 becomes

$$P(\vartheta|y_t) \propto \int P(y_t|x_t, \theta)P(x_t|\theta)P(\theta|\vartheta)P(\vartheta) d[x_t]d\theta \quad (11)$$

If  $[x_t, y_t]$  is Markovian, then path integration can be equivalently transformed into filters as follows:

$$\int P(y_t|x_t, \theta)P(x_t|\theta)P(\theta|\vartheta)P(\vartheta) d[x_t] = \int P(y_t|y_{t-1}, x_t, \theta)P(x_t|x_{t-1}, \theta)P(y_{t-1}|x_{t-1}, \theta) dx_t P(x_{t-1}|\theta)P(\theta|\vartheta)P(\vartheta)d[x_{t-1}]d\theta \quad (12)$$

Hyper-parameters can greatly reduce the number of variables to be inferred and so relieve the over-determination. However, it is essential to identify the hyper-parameters as well as the parametric distribution of the parameters, towards balancing between overfitting and preciseness of models.

#### *BOLD signal model*

Towards a Bayesian inference, the mathematical model is based on the neuronal network model and a hemodynamical model that takes the neural activity quantified by the spike rate of a pool of neurons and outputs a Bold signal. Let  $z_t$  be the time series of neural activity and the hemodynamical model can be generally written as

$$\dot{g} = G(g, z)$$

Here  $g$  denotes the states related to blood volume and blood oxygen consumption. And the bold signal is read as a function of  $g$ , i.e.,  $y(t) = h(g(t))$ . There are diverse hemodynamical models and herein, we introduce the Balloon-Windkessel model (11) (table S2). The neural activity of each pool of neurons associated with the ROI/voxel is the input ( $z_i$ ) and  $y_i(t)$  with down-sampling coinciding with the frequency of fMRI scanning.

#### *Hierarchical mesoscale data assimilation (HMDA)*

We take each ROI as the subnetwork and assume that the conductance parameters of the same type of the neurons in the same ROI follow the same distribution, or equivalently, share the same hyper parameters. The time series of the BOLD signal from the ROI are formulated by the Balloon-Windkessel model mentioned above, and taken as the observations. The aim of the data simulation is to estimate the hyperparameters  $t$  of all ROIs by tracking the BOLD signals. In practice, the parameter inference is realized by the ensemble Kalman filter and the hyperparameter inference (Eq. 11) is realized by a simple random-walk bootstrap filter. Consider the following general evolution equations:

$$\begin{cases} x(t) = G(x(t-1), \theta(t-1)) + \varepsilon_g \\ z(t) \leftarrow SpN(x(t)) \\ r(t) = BW(z(t-1), r(t-1), \theta(t-1)) \\ y(t) = Hr(t) \\ \theta(t) = cdf^{-1}(cdf(\theta(t-1), \vartheta(t-1)), \vartheta(t)) \\ \vartheta(t) = \vartheta(t-1) + \varepsilon_\vartheta \end{cases} \quad (13)$$

Here,  $x(t)$  stands for the state variables (membrane potentials and synaptic currents) of all neurons in the whole-brain neuronal network model,  $G(\cdot)$  gives the discrete-time integrals of

Eq. 9 and  $\varepsilon_g$  stands for the white Gaussian noises which are injected into the membrane potential equations;  $SpN(\cdot)$  gives the threshold model of registering spike trains from the membrane potentials,  $z(t)$  gives the neural activity (measured by spike counts) of each ROI;  $BW(\cdot)$  gives the Euler discrete-time version of the Balloon-Windkessel model with  $r(t)$  for its state variables, and  $y(t)$  stands for the BOLD signal generated by the Balloon-Windkessel model;  $\theta(t)$  stands for all parameters in the models that are to be estimated and  $\vartheta(t)$  for the corresponding hyperparameters;  $cdf(\cdot)$  stands for the cumulant distribution function of the parameters (alternatively the empirical distribution if taking them by bootstrap method, for example Monte-Carlo Markov Chain (MCMC)); the hyperparameters evolve by random walks.

The iterative Bayesian inference from observed data to the states and parameters is conducted by the standard ensemble Kalman filters. Herein, we utilize two alternatives of ensemble Kalman filter (EnKF) methods. The first one is the standard ensemble Kalman filter with the pseudo codes (Algorithm 3).

---

**Algorithm 3** Ensemble kalman filter

---

**Input :**

ROI-wise BOLD signals  $y_t, t = 1 \dots T$ ;  
number of total samples  $N$ ;  
total time length  $T$ ;  
initial state and initial estimation;

**Output :**

estimated BOLD signals;  
hidden states and parameters;

- 1: Draw  $N$  samples  $x_0^n$  from initial distribution;
  - 2: **for**  $t = 1 : T$  **do**
  - 3:   evolve state  $\hat{x}_{t-1}^n$  to  $\hat{x}_t^n$  respectively
  - 4:   calculate  $\mu_t = \frac{1}{N} \sum \hat{x}_t^n, C_t = \frac{1}{N-1} \sum (\hat{x}_t^n - \mu_t)(\hat{x}_t^n - \mu_t)^T$ .
  - 5:   derive Kalman gain matrix  $S_t = HC_tH^T + \Gamma_o, K_t = C_tH^T S_t^{-1}$
  - 6:   filter by  $x_t^n = \hat{x}_t^n + K_t(y_t - \epsilon_o^n - H\hat{x}_t^n)$
  - 7: **end for**
- 

The second one is the diffusion ensemble Kalman filter. The computation complexity of each iteration depends on the dimension of the observed data. In the case of experimental observations with high resolution, the dimension of  $y$  can be very high, which may cause both computation complexity and ill-posedness due to the limited number of data time points. The distributed Kalman filter is an efficient way to handle high-dimensional observations (46). Taking each observer as an independent sensor, a fusion process is added to correction of each sensor by weighted average. Herein, we utilize this idea to the diffusion EnKF by taking each ROI bold signal as an observer and establishing an independent EnKF (Algorithm 4). Correction of the states, parameters and hyperparameters of this ROI is weighted average between EnKF of itself and EnKF from other ROIs (47). A fusion coefficient  $\gamma$  is introduced to balance the fusion of corrections from this ROI and all other ROIs.

---

**Algorithm 4** Diffusion ensemble kalman filter

---

**Input :**

ROI-wise BOLD signals  $y_t, t = 1 \dots T$ ;  
number of total samples  $N$ ;  
total time length  $T$ ;  
initial state and initial estimation;  
fusion coefficient  $\gamma$ ;  
dimension of observation state  $L$  (equals to number of ROIs);

**Output :**

estimated BOLD signals;  
hidden states and parameters;

- 1: Draw  $N$  samples  $x_0^n$  from initial distribution;
  - 2: **for**  $t = 1 : T$  **do**
  - 3:   evolve state  $\hat{x}_{t-1}^n$  to  $\hat{x}_t^n$  respectively.
  - 4:   calculate  $\mu_t = \frac{1}{N} \sum \hat{x}_t^n, C_t = \frac{1}{N-1} \sum (\hat{x}_t^n - \mu_t)(\hat{x}_t^n - \mu_t)^T$ .
  - 5:   derive Kalman gain matrix  $S_t^l = H_l C_t H_l^T + \Gamma_{o,l}, K_t^l = C_t H_l^T (S_t^l)^{-1}$ .
  - 6:   filter by  $x_{t+1/2}^{n,l} = \hat{x}_t^n + K_t^l (y_t - \epsilon_o^{n,l} - H_l \hat{x}_t^n)$  for  $l = 1 \dots L$ .
  - 7:   correct  $x_t^{n,l}$  based on  $x_{t+1/2}^{n,l}$ :  $x_t^n = \text{diag}(x_{t+1/2}^n \Upsilon(\gamma))$ ,
  - 8:   where  $x_{t+1/2}^n = [x_{t+1/2}^{n,l}]_l$  and  $[\Upsilon(\gamma)]_{i,j} = \gamma$  if  $i=j$  else  $\frac{1-\gamma}{L-1}$ .
  - 9: **end for**
- 

Thus, we are to establish a framework for HMDA of fMRI over the neuronal network and hemodynamic models by taking all states of neuronal including neural activities (spikes), synaptic currents, variables of hemodynamics, bold signals, and the parameters to be estimated as well as its preassigned distribution with the hyperparameters. Analysis and prediction of the HMDA filter is executed at each time point of the BOLD signals. The time scale follows the biological clock (in ms) and taking each time step as the period of the fMRI scanning. We utilize the diffusion ensemble Kalman filter for the population of state and parameter inference, which gives the framework of distributed hierarchical mesoscale data assimilation (dHMDA). In the following work, we take the hyper-parameters of the synaptic conductance  $g_{u,i}$  in Eq. 3 to statistically infer the model with the resting-state fMRI data and those of the external current  $I_{ext,i}$  in Eq. 1 to statistically infer the model with task fMRI data.

Although HDMA takes consideration of all hidden states and parameters contained in model, what we want is that the network driven solely by the synaptic conductance. Therefore, after estimating the hyperparameter of subnetwork with observation signal (experimental BOLD signal), we re-simulate this model by assigning synaptic conductance for each neuron according the hyperparameter series ( $g_u$ ) and then evaluate fitting effect. The resting-state and task-state fitting results of the whole-brain model demonstrate the validity of our proposed HDMA algorithm.

*Layout of HDMA on GPU HPC*

The layout of data assimilation is logically composed of two classes of units: each simulation worker may be physically a part of computation hardware (a GPU, several GPUs and several nodes) and simulates a single model of DTB; a HMDA worker conducts the HDMA according to the simulated data and the observation data. In our layout, towards a better performance, we layout the iteration of the parameters according to the hyperparameters, i.e., the fifth item in

Eq. 13 onto the GPU simulation worker, since it is of parallel high load of computation. Besides a centralized HDMA worker based on the standard HMDA, alternatively, we also utilize the dHMDA by setting  $m$  (equal to the number of ROIs or voxels) HDMA workers and conduct the fusion processing (the last step in algorithm 4) at each HDMA worker.

The GPU simulation worker iteratively samples the parameters of its WBNN model from the hyperparameters, simulates neuron states, and send the neural activities (in term of spike counts or rates) to the CPU HDMA worker (fig. S6). The HDMA worker takes the hyperparameters and the state variables of the hemodynamics into the ensemble Kalman filter, which in facts assumes that the evolution of the state variables of the neuron model given the parameters and the parameters induced by the hyperparameters are precise. The HMDA worker simulates the hemodynamics, outputs the bold signals, conducts HMDA filter or dHMDA of each iteration, and send the iterated hyperparameters to the simulation workers.

### *Correlation coefficients*

We mainly use the Pearson correlation coefficients between the simulation DTB after data assimilation and the experimental fMRI data in voxels to measure the performance of the DTB. Since the ensemble Kalman filter tracks the real data usually with small delays, we alternative employ the following lag correlation coefficients:

$$pcc(x_{DTB}(t + lag), x_{exp}(t))$$

where  $pcc(\cdot, \cdot)$  stands for the Pearson correlation coefficients,  $x_{DTB,exp}$  for the time course acquired by the DTB and experimental counterpart and  $lag$  for the time delay. We take  $lag = 4$  throughout the paper if without special annotations.

### ***Biological data acquisition***

For illustration, we scan multi-model MRI from the corresponding author of this paper, Jianfeng Feng (i.e., JF data). All neuroimaging was performed on a 3 Tesla MR scanner (Siemens Magnetom Prisma, Erlangen, Germany) at the Zhangjiang International Brain Imaging Centre in Shanghai, using a 64-channel head array coil. High-resolution T1-weighted (T1W) MR images were acquired using a 3D Magnetization-Prepared RApid Gradient Echo (3D-MPRAGE) sequence (TR/TE = 3000/2.5 ms, TI = 1100 ms, FOV = 256 mm, flip angle = 7°, matrix size = 320 x 320, 240 sagittal slices, slice thickness = 0.8 mm, no gap). Multi-shelled, multi-band diffusion-weighted images (DWI) were acquired using a single-shot spin-echo planar imaging (EPI) sequence (monopolar scheme, TR = 3200 ms, TE = 82 ms, Matrix size: 140x140, voxel size: 1.5 x 1.5 x 1.5 mm<sup>3</sup>, multiband factor = 4, phase encoding: anterior to posterior) with two b-values of 1500 s/mm<sup>2</sup> (30 diffusion directions) and 3000 s/mm<sup>2</sup> (60 diffusion directions), in which b0 images were interleaved in every 6 volumes. Each volume consisted of 92 contiguous axial slices (thickness: 138 mm). Data with the same DWI protocol using an opposite polarity (phase encoding from posterior to anterior) were also acquired. Resting-state and task state fMRI were acquired using a gradient echo-planar imaging (EPI) sequence (repetition time, TR: 800 ms, echo time, TE: 37 ms, field of view, FoV: 208 mm, flip angle: 52 degrees, matrix size: 104x104x72, and voxel size: 2 x 2 x 2 mm<sup>3</sup>, multiband factor = 8, phase encoding: anterior to posterior). The resting-state fMRI scan consisted of 488 contiguous EPI volume and each task state fMRI scan has two runs, which consisted of 487 EPI volume, respectively.

### **Supplementary Text:**

### ***Biological data preprocessing***

T1w data were preprocessed with the voxel-based morphometry (VBM) by using the VBM8 toolbox based on the Statistical Parametric Mapping (SPM, <http://www.fil.ion.ucl.ac.uk/spm>). Firstly, all structural MRI data were manually corrected and divided into grey matters, white matters and cerebrospinal fluid. Secondly, the grey matter images were aligned to a nonlinear deformation field and normalized to Montreal Neurological Institute (MNI) space by using the templates which were created by DARTEL tool. Finally, the normalized images were all smoothed with a full-width at half-maximum (FWHM) 8-mm Gaussian kernel for further analysis. After above procedures, the grey matter images were resampling at a resolution of  $3 \times 3 \times 3\text{mm}^3$ .

FSL software V6.0.4 (Functional Magnetic Resonance Imaging of the Brain Software Library, <http://www.fmrib.ox.uk/fsl>) and MRtrix 3.0 (<http://www.mrtrix.org/>) (48) was utilized to preprocess DWI data (49). The DWI was denoised and corrected for Gibbs ringing artifacts (50-53). The DWI was then corrected for head motion, eddy current, and tissue susceptibility-induced off-resonance geometric distortions with the reversed phase encoding  $b = 0$  s/mm<sup>2</sup> images (54-57). The DWI bias field created by the nonuniform coil receives sensitivity was also corrected (58, 59). For the the anatomical connectivity matrix, we firstly generated a mask image appropriate for seeding streamlines on the grey matter-white matter interface. White matter tractography was used to estimate the fiber tract numbers connecting each pair of voxels in the mask image, resulting in an anatomical connectivity matrix. The connection of a voxel to itself was set to 0 in the connectivity matrix for the simulations.

For BOLD signals, the following preprocessing was performed using *fMRIPrep* (60). First, a reference volume and its skull-stripped version were generated using a custom methodology of *fMRIPrep*. A deformation field to correct for susceptibility distortions was estimated based on *fMRIPrep's fieldmap-less* approach. The deformation field is that resulting from co-registering the BOLD reference to the same-subject T1w-reference with its intensity inverted (61). Registration is performed with *antsRegistration* (ANTs 2.3.3), and the process regularized by constraining deformation to be nonzero only along the phase-encoding direction, and modulated with an average fieldmap template (62). Based on the estimated susceptibility distortion, a corrected EPI (echo-planar imaging) reference was calculated for a more accurate co-registration with the anatomical reference. The BOLD reference was then co-registered to the T1w reference using *flirt* (63) with the boundary-based registration (64) cost-function. Co-registration was configured with nine degrees of freedom to account for distortions remaining in the BOLD reference. For resting-state data, ICA-based automatic removal of motion artifacts (AROMA) was used to generate aggressive noise regressors as well as to create a variant of data that is non-aggressively denoised (65). Then the preprocessed data were smoothed with a full width at FWHM Gaussian kernel of 6 mm and filtered with a band-pass filtering (0.01 – 0.1 Hz). Finally, the preprocessed data were resampling at a resolution of  $3 \times 3 \times 3\text{mm}^3$ .

### ***Digital twin brain (DTB) with visual stimulus***

Under the best fitted DTB, we explore how visual information is propagated in the brain network model with 200 million neurons including a micro-column structure. A pulsed electrical stimulus with duration = 50 ms and intensity = 0.6 mA is employed to the excitatory neurons in the voxels of the visual brain regions (Calcarine in the AAL template) in the specific time interval (50 ms) to mimic the transcranial random noise (34).

We then collect both the micro-level data including local field potential (LFP) and spike trains, generated by averaging the membrane potentials of the neurons in the interested voxels and micro-columns, and the macro-level data, including the BOLD signals generated by the hemodynamic models, from the simulation of the neuronal network, towards comparing the dynamics before and after visual stimulus. We use three methods to analyze the information flows between brain regions in the whole brain.

The first one is simply ranking the onset time of evoked spikes in brain regions of interests with respect to the stimuli. Second, once perturbation of the response is halted, we use the measure—the average activation strength which is defined as the integral mean value between the curves of integration value (50 ms window) over time for perturbed dynamics (post-stimulus state) compared to the basal state dynamics (pre-stimulus state) (25), to evaluate the stimulus response of a voxel. Specifically, we perform a permutation test approach to implement Wilcoxon rank Sum Test ( $p > 0.005$ ). From Figure S7, one can see that the results of auditory stimulation experiment confirm the pathway of auditory information transmission. Furthermore, a novel computational framework is established to explore the information flow based on the simulated LFP signals, which calculates the velocity vector field of the hidden brain dynamics for each millisecond involving both the spatial and temporal information. Specifically, the simulated local field potential signals are bandpass filtered (10-30 Hz) and then transformed to MNI152 space prior to surface mapping. Then the preprocessed data are mapped to cortical surface meshes using the standard Human Connectome Project pipeline. Finally, the resulted time series are aligned to 32k fs\_LR atlas space. The velocity vector field is calculated by adapting optical flow estimation methods with a spatial total variational penalty. Concretely, given a signal  $I(\mathbf{x}, t)$ , the velocity field of the hidden dynamics can be extracted by solving the following inverse problem as:

$$\begin{aligned} \min_{u \in \Omega} \sum_x |I_x \cdot u + I_t| + \rho \sum_x \|\nabla u\|_{l_2} \\ \text{s. t. } u = 0 \text{ outside } \Omega \end{aligned} \quad (14)$$

where  $\Omega$  denotes the whole region with effective LFP signals and the regularization parameter in this model is taken as  $\rho = 0.001$ . Moreover, this convex optimization is solved by the GADIM algorithm (66).

### ***DTB for deep brain stimulus (DBS)***

We perform the digital experiments on Feng’s digital brain by setting DBS to given brain ROIs. The simulated results provide insights into the influence of DBS on whole brain. In the section, we use the whole-brain computational model of resting-state brain, composed of 100 million neurons and 22705 voxels with a minor modification. The left and right subthalamic nucleus (STN) are chosen as the stimulus sites.

The DBS stimulus is mimicked by a pulse current (frequency = 125Hz, mean amplitude = -6 mA, pulse width = 1ms), which is injected to all neurons in the STN voxels with the amplitudes following the distribution of  $-\text{Gamma}(5, 6/5)$  statistically interpedently. For statistical analysis, we carry out 100 repetitive trials of the digital DBS experiments. Each simulation trial is composed of 80 seconds’ simulation: the first 40 s as the resting-state and the last 40 s with applying DBS stimulus. We record the instantaneous firing rate and local filed potential in millisecond. In particular, the LFP is estimated by the mean of four synaptic currents (AMPA, NMDA, GABAa and GABAb) of all neurons in the ROIs. For the removal of

stimulation artifacts, the raw LFP is preprocessed through the Chebyshev filters (type I) to filter the frequency over 100 Hz. The time-frequency spectrum is obtained by Morlet wavelet transform. The power spectral density (PSD) is estimated by the Welch's overlapped segment averaging estimator.

In this experiment, except for STN, five Parkinson's disease-related brain regions (29) are selected to perform further analysis. For each ROI, the voxel with largest structural connection with STN is firstly picked and the spatially adjacent voxels with structural connection to STN are also included. Finally, 22 voxels are picked out in thalamus (THA), 21 voxels in supplementary motor area (SMA), 13 voxels in precentral gyru (PreCG), 8 voxels in caudate (CAU) and 10 voxels in putamen (PUT). To investigate the effects of DBS on the neural circuits, the Granger causality among six ROIs is calculated with the ROI-averaged filtered LFPs (30, 31). The order of the model is 1 (10ms) estimated by Bayesian Information Criterion (BIC). The statistical results are estimated by averaging over 100 repetitions.

Finally, this platform provides the possibility to explore the optimal parameters of DBS and its underlying mechanism. We perform the DBS digital experiments with two kinds of DBS stimulus setup. First, we fix the pulse width, as 1ms, with respect to different frequencies: 10Hz, 50Hz, 75Hz, 100Hz, 125Hz and 200Hz. Second, we fix the quantity of electricity for the stimulus duration (40 secs) with respect to different frequencies 10Hz, 50Hz, 75Hz, 100Hz, 125Hz and 200Hz, as well. In order to keep the same quantity of electricity equal to 0.0012 C, in the present experiment, we set different pulse widths for the DBS stimulus respectively. For instance, we set 1ms pulse width for 200 Hz DBS, and 20 ms pulse width for 10Hz DBS. In addition, we introduce the percentage decrease of  $\delta, \theta$ -rhythms of the LFP, defined as follow:

$$\frac{\langle PSD \text{ at rest} - PSD \text{ at DBS} \rangle_{\delta, \theta}}{\langle PSD \text{ at rest} \rangle_{\delta, \theta}} \quad (15)$$

where  $\langle \cdot \rangle_{\delta, \theta}$  stands for average over all rhythms of  $\delta, \theta$ -rhythms of the LFP and “at rest” and “at DBS” means to calculate the PSD over the resting-state duration (the first 40 s) and the DBS duration (the last 40 s) respectively.

### ***DTB for appetitive/aversive evaluation prediction***

Based on human-scale brain neuromorphic simulation and data assimilation method on the voxel-wise MRI, in the present paper, we conduct an explorative step towards establishing a digital brain model and methodologies that can assimilate the model with the experimental data and the infer the perceptive and cognitive tasks. Due to the complexity of visual and auditory perception, there is no good encoding and decoding model to replace this process. DTB approximates the input signal of the input region by assimilating the BOLD signal acquired from experiment, and then simulates the propagation of the signal within best-fitted resting brain. Finally, we extract the signal of the decision regions (all voxels excluding the input regions) and makes the score prediction. The detailed results of evaluation prediction on auditory task can be seen in Fig. S8.

We design perceptual and cognitive task experiments and collect the voxel-wise BOLD signals for assimilating the digital brain model. Herein, we consider the visual and auditory evaluation task. The experiment consisted of three emotional runs (positive run, negative run, and neutral run). Each run has 20 emotional figures or sounds, which was present for 3 seconds. Then the participants were asked to evaluate how they feel to the stimulus with a Likert scale from (0 – 10) in 4 seconds.

To assimilate DTB in action, we first utilize the resting-state digital brain model on JF data as the initial state to assimilate the experimental data of the tasks. According to the specific task, we assimilate the perceptive ROIs by the task fMRI data in the whole brain neuronal network. We employ the dHMDA on the perceptive ROIs at the voxel level and the assimilated hyper-parameters of injection currents of the voxels in the perceptive ROIs will serve as the “input” brain ROIs. For instance, in the visual evaluation experiment, we consider the voxels in the calcarine (CAL), inferior frontal gyrus (opercular part, IFGoperc), and supramarginal gyrus (SMG) in AAL template as the visual input ROIs. (The CAL is responsible for the primary visual information processing. The IFGoperc mediates active maintenance of stimulus information. The SMG is part of the somatosensory association cortex, which receives somatosensory, visual, and auditory inputs from the brain).

To explore the potential applications of DTB in cognitive decision making, we use DTB to virtually mimic the real-world experiment, which JF really did but another subject did not really execute, and then predict the performance. Specifically, for another subject (named subject B), we firstly establish the whole-brain neuronal network model based on her/his structural MRI data and then assimilate the hyper-parameters of the synaptic conduces of each voxel in subject B with her/his resting-state fMRI. With the AAI template, we align the voxels of subject B to JF. We deploy the assimilated hyper-parameters of the injection currents of the voxels in the perceptive input ROI for subject B to sample the injection currents of the voxel in the perceptive input ROI of the same location from the hyper-parameters of JF. Hence, we simulate the whole-brain neuronal networks for subject B to virtually and digitally mimic the digital task experiment as JF really did.

The brain activation for each trial was assessed with both the biological and digital BOLD signals by the general linear model, in which the regressors for modeling each trial was established by convolving the corresponding experimental condition with SPM’s canonical hemodynamic response function (HRF) and six head motion parameters were as the additional covariate regressors. Hence, the patterns of brain activation were comparable between the digital brain and biological brain. Furthermore, we take brain activations during stimuli evaluation as the response variables and scores of pictures as the predictors in a linear regression model. The least absolute shrinkage and selection operator (LASSO) regularization is employed to pursuit a sparse coefficient vector. The picture evaluation task of each subject involves 18 pictures. We exclude the first two trails due to the quality of assimilation and removed the duplicated trails with the same stimulus. The leave-one-out approach is applied to measure the performance. That is, we take the brain activations of all voxels excluding the ones in input regions and scores of each 17 pictures as training data to estimate a sparse coefficient vector via LASSO. Then we use this coefficient vector and the brain activations during evaluation of the remaining one to predict how the subjects score this picture.

# Supplementary Figures and Tables

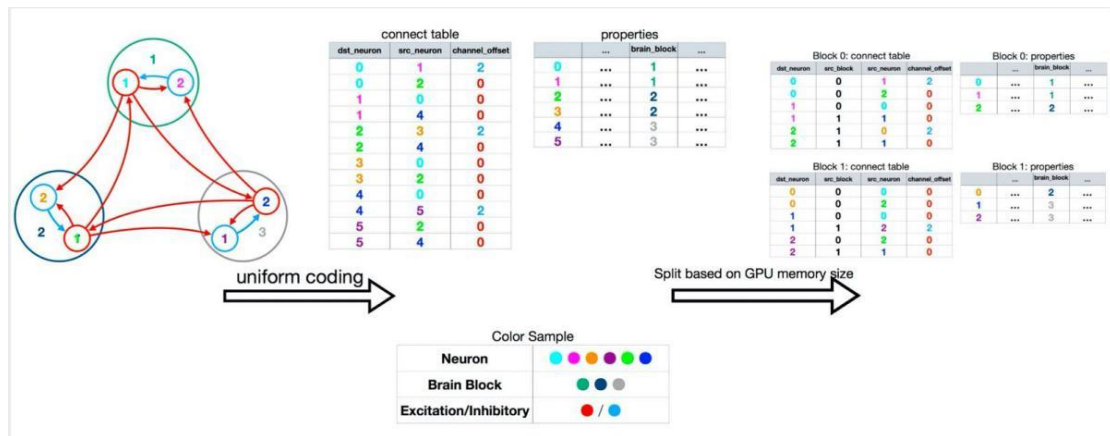
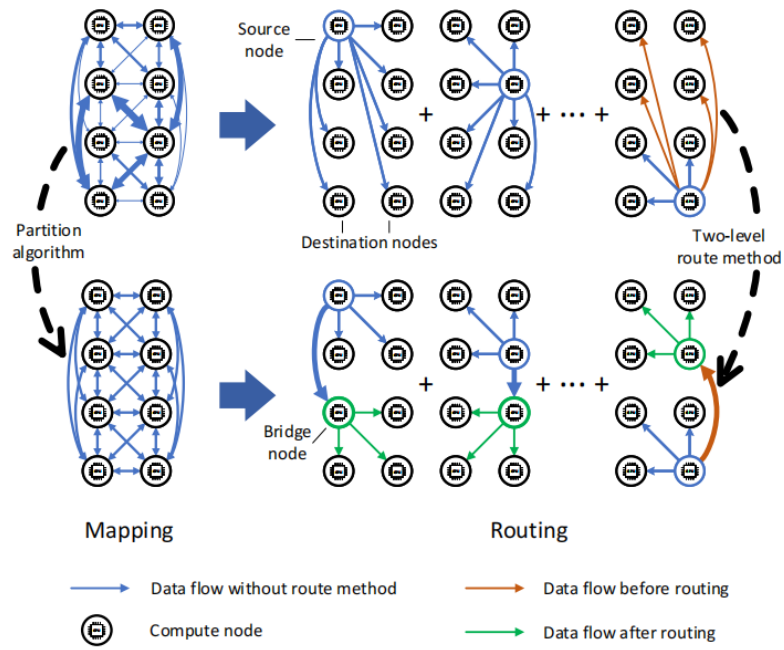
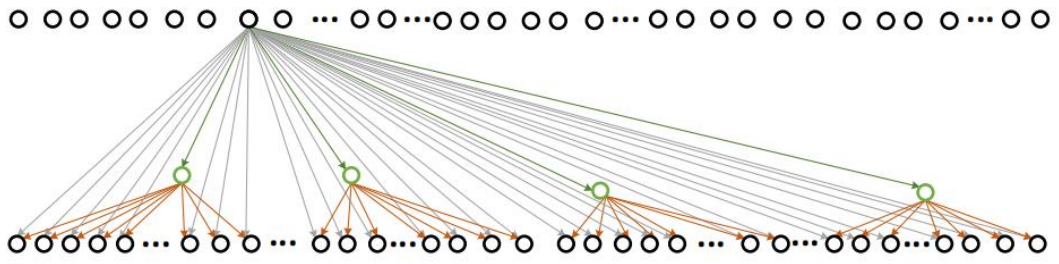


fig. S1 The link table and spike communication organization.



**fig. S2 Illustration of the partition algorithm and routing method.**



**fig. S3 Illustration of the two-level routing method.**

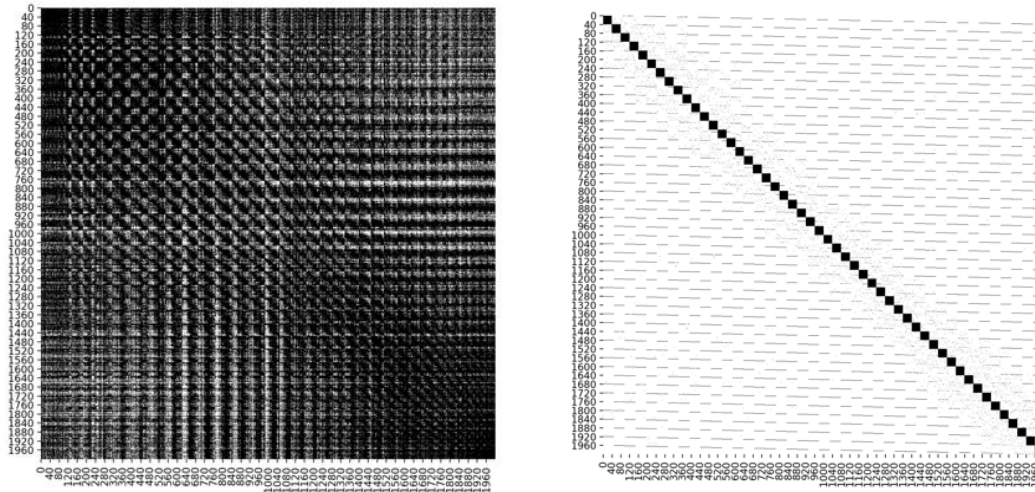


**fig. S4 Real connections during the communication of 2000 GPUs.** (left panel) The connections between GPUs without two-level routing method; (right panel) The connections between GPUs with two-level routing method

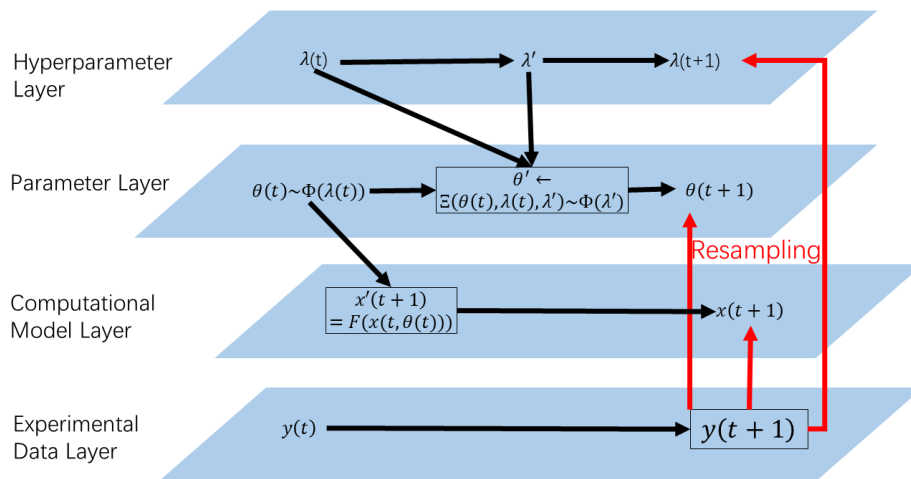


**fig. S5 Framework of Hierarchical Bayesian Inference.**

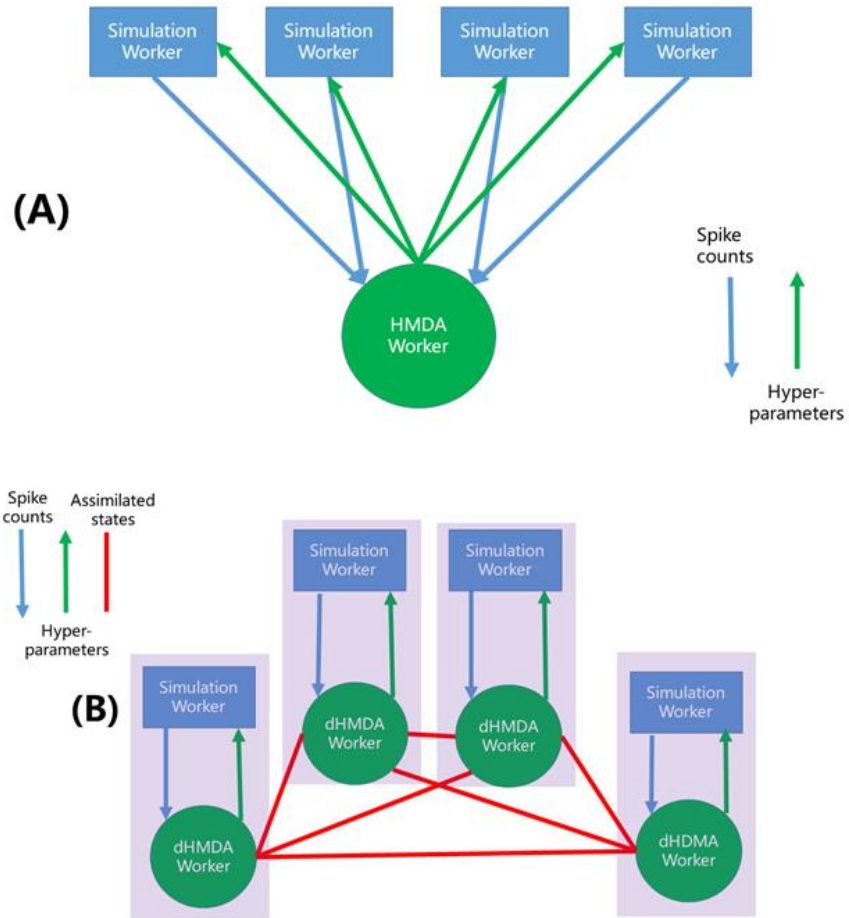


**fig. S6** Layout framework of HMDA (A) and dHMDA (B) for fMRI data.

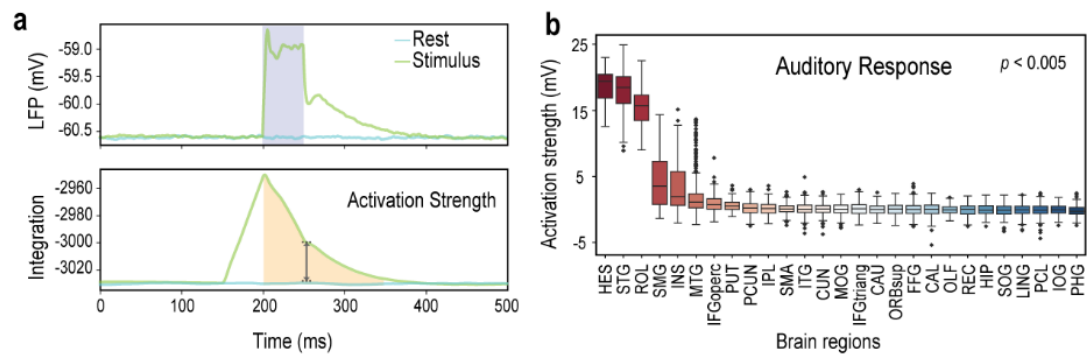


**fig. S7. Auditory stimulus results.** (a) The definition of average activation strength of a voxel after the pulse stimulus. (b) Significantly activated brain regions order ranked by its average activation strength in auditory stimulus experiment.

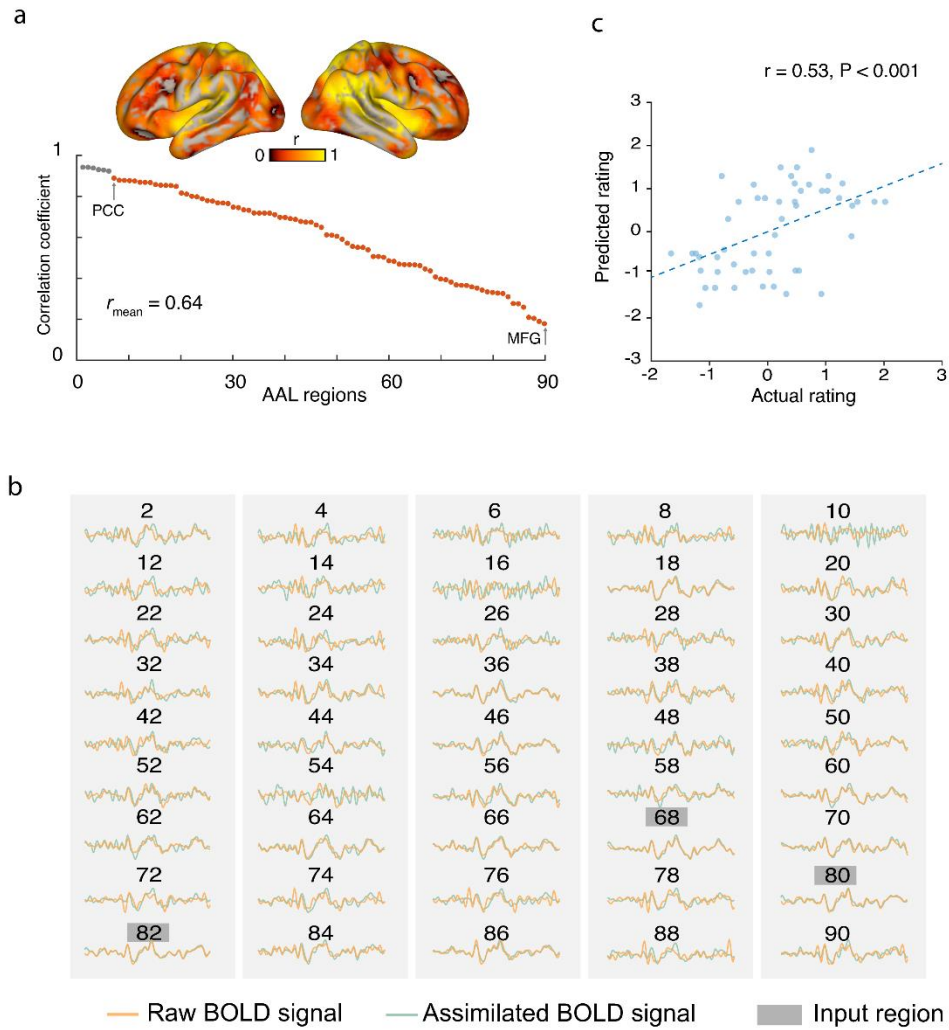


**fig. S8. DTB in action (auditory experiment).** (a)The whole-brain voxel-level correlation analysis. (b)The time course of assimilated BOLD signal and raw BOLD signal for each right hemisphere AAL region (lag = 4) of auditory evaluation task. (c)The predicted performance based on the assimilated fMRI data.

		presynaptic										
		i1	e2/3	i2/3	e4	i4	e5	i5	e6	i6	CC	
postsynaptic	e1	1323	823	200	15	1	9					10133
	i1	901	560	149	10	1	6					6899
	e2/3	133	3554	804	881	45	431		136			1020
	i2/3	52	1778	532	456	29	217		69			396
	e4	27	417	84	1070	782	79	8	1686			1489
	i4		168	41	628	538	36		1028			790
	e5	147	2550	176	765	99	621	596	363		7	1591
	i5		1357	76	380	32	375	403	129			214
	e6	2	643	46	549	196	327	126	925	597		2609
	i6		80	8	92	3	159	11	76	499		1794

**table S2. Average number of synapses received by individual neuron in each cortical layer.** e1,2/3,4,5,6 and i1,2/3,4,5,6 stand for the excitation and inhibition neuron population of the layer 1,2/3,4,5,6 respectively.

Equations	Notations
$\dot{s}_i = z_i - \kappa_i s_i - \gamma_i (f_i - 1)$	$z_i$ the neural activity; $s_i$ vasodilatory signal; $i$ the label of ROI/voxel
$\dot{f}_i = s_i$	Inflow
$\tau_i \dot{v}_i = f_i - v_i^{\frac{1}{\alpha}}$	Blood volume; $f_{out,i} = v_i^{\frac{1}{\alpha}}$
$\tau_i \dot{q}_i = \frac{f_i E(f_i, \rho_i)}{\rho_i} - v_i^{\frac{1}{\alpha}} q_i / v_i$	Deoxyhemoglobin content, $E(f, \rho) = 1 - (1 - \rho)^{\frac{1}{f}}$
$y_i = V_0 [k_1 (1 - q_i) + k_2 \left(1 - \frac{q_i}{v_i}\right) + k_3 (1 - v_i)]$	Bold signal

**table S2 Details of the Balloon-Windkessel model.**

# Supplementary Report:

## Simulations of a Human-Brain Scaled Neuronal Network of 86 billion Neurons

### Abstract

We have conducted neuromorphic simulation of leakage-integrate-fire (LIF) neuronal networks of 86 billion neurons with network structure from Feng Jianfeng's MRI data (T1 and DTI) combined with micro-column model on cortex. With 1 ms time-step, we achieved the time-to-solution (ToS) around 60 on the HPC with 10000 GPUs. We also simulated the assimilated model over the resting-state voxel-wise BOLD signals. The DTB showed a good coherence with the biological counterparts.

### Experiment Setup

We completed digital twin brain (DTB) experiments that simulated up to 86 billion neurons network, which corresponds to the full size of the human brain, on the 2500 heterogeneous computing nodes supercomputer. To accelerate computer simulation, graphics processing units (GPUs) as special-purpose hardware for parallel computing provide tremendous computational power for simulation. Every supercomputer node is composed of 32 processor cores hosted on a multi-core CPU and 4 GPUs each with 16GB memory. Among these nodes a 200Gbps bidirectional Infiniband network is connected. DTB applications run on 4 of 32 processors, each consisting of a single process that utilizes a separate GPU. Thus, we were able to run the DTB experiment in the 160 TB GPU memory of the system.

### Results

The human brain model in DTB consists of 86 billion neurons (80% excitatory) and 100 average synapses per neuron. Each neuron is described by the Leaky integrate and fire (LIF) model with four synaptic currents (AMAP, NMDA, GABAA, GABAB). The structural connection probability between neurons is according to the Diffusion Tensor Image (DTI) and micro-column neuroanatomy data. To reduce communication time, we apply the partitioning algorithm to assign a set of neurons with high communication demands on the same GPU due to the faster communication speed within the GPU. The neurons and their synapses at each GPU are coded in a single link table, including the attributes (parameters) of each neuron, which are used to evolve its membrane potential; and the attributes of each synapse, composed of the label of neurons coming from and going to (neuron index and GPU block index), and the type of synapse and its synaptic weights. The initialized procedure of DTB not only generates the link tables, which are up to 115T and stored in the physical store but also assigns the information of link tables on different GPUs. Since the human

brain model in DTB is heterogeneous, each GPU-loaded memory is still not balanced even after applying the partitioning algorithm (shown in Figure 1). Finally, we were able to simulate 3000 ms of DTB human brain model time with a simulation time step of 1 ms. For counting the amount of communication data in the simulation, we add statistical interfaces in our software, which would change some of calculation and communication from parallel to serial, resulting in reducing the speed of the simulation. To distinguish whether to add interfaces or not, we name the two software as benchmark and benchmark with statistics respectively. Several experiments are shown in Table 1, where the most efficient one was achieved by simulating 1 ms biological time in 60 ms of real-time, at a mean firing rate of 17.5 Hz (shown in Figure 2).

Actually, the time to solution of simulating depends on the amount of computation of synaptic conductance and communication data of spike information while the latter depends on the firing rates in the network. In DTB, combined with BOLD signals (blood oxygen level dependent signals) from fMRI scanning, we utilized the hierarchical brain assimilation method to correct synaptic conductance parameters in the model, so that our brain model could adjust the firing rate. More specifically, hierarchical brain assimilation estimates the parameters by iterating two processes: simulation, computing the hidden states including model parameters and states by numerical calculation, and assimilation, adjusting the model hidden states by data assimilation (DA) methods such as ensemble Kalman filter (EnKF) according to BOLD observation. After hierarchical brain assimilation, Pearson correlations between the empirical and assimilated BOLD signals at the brain region resolution is 0.90 at a mean firing rate of 10 Hz. The sum of messages communicated between GPUs during 1s simulation time is up to 43TB, and the distribution of communication data on each GPU is shown in Figure 3.

	<b>software</b>	<b>size</b>	<b>input noise</b>	<b>firing rate</b>	<b>simulation time</b>	<b>wall-clock time</b>	<b>Time of solution</b>
1	benchmark	86billion	10Hz	17.5Hz	3s	180s	60
2	benchmark	86billion	10Hz	17.5Hz	3s	228s	76
3	benchmark with	86billion	10Hz	6.6Hz	3s	207s	69

	statistic						
4	benchmark with statistic	86billion	10Hz	17.5Hz	3s	232s	77

**Table 1** shows several experiments using different software. In the DTB brain model, each neuron received 10Hz noise spikes as random input to prevent the silent state. We adjust initial synaptic conductance parameters to vary the firing rate from 6.6Hz to 17.5Hz. Time-to-solution of the most efficient experiment is 60 based on benchmark software, at a mean firing rate of 17.5 Hz.

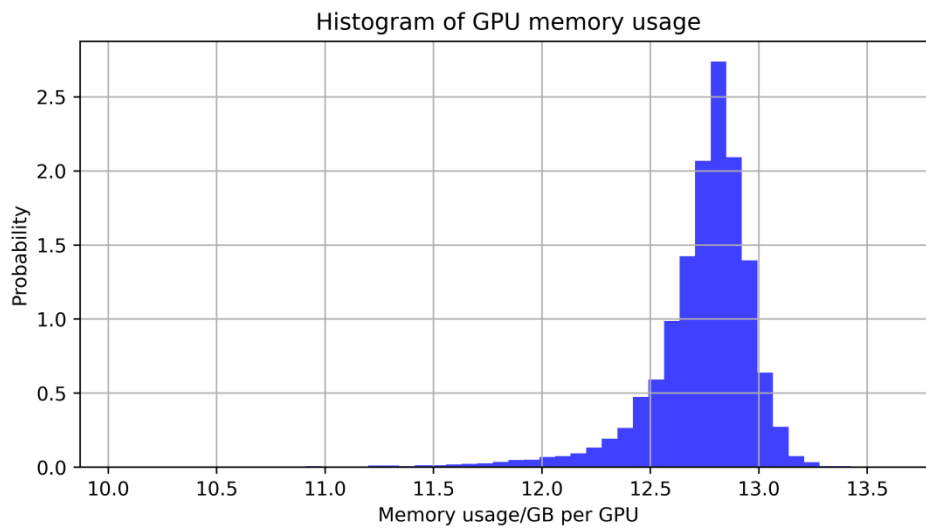


**Figure1** shows the distribution of actual GPU memory usage after applying partitioning algorithm.

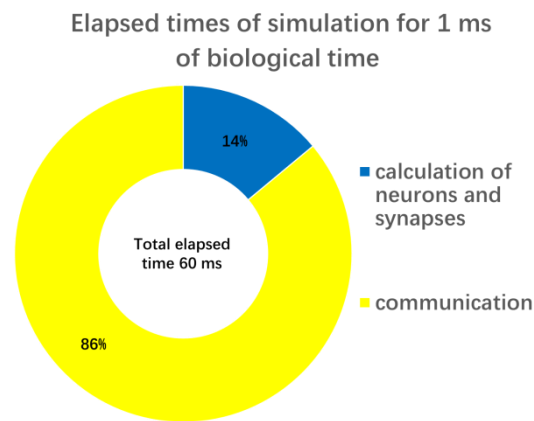


**Figure 2** shows elapsed times of simulation for 1 ms of biological time: calculation of neurons and synapses (blue), and communication (yellow).

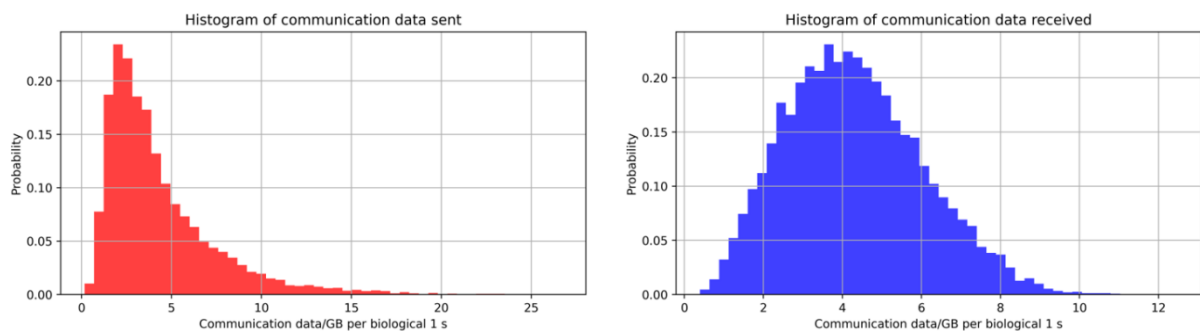


**Figure 3** shows the distribution of communication data during simulating for 1 s of biological time: sent by nodes (red), and received by nodes (blue).